



**HAL**  
open science

# **A new interpolation method to measure delta evolution and sediment flux: Application to the late Holocene coastal plain of the Argens River in the western Mediterranean**

Jean-Philippe Degeai, Frédérique Bertoncello, Matteo Vacchi, Laurent Augustin, Alain de Moya, Luigi Ardito, Benoît Devillers

## **► To cite this version:**

Jean-Philippe Degeai, Frédérique Bertoncello, Matteo Vacchi, Laurent Augustin, Alain de Moya, et al.. A new interpolation method to measure delta evolution and sediment flux: Application to the late Holocene coastal plain of the Argens River in the western Mediterranean. *Marine Geology*, 2020, 424, pp.106159. 10.1016/j.margeo.2020.106159 . hal-02911834

**HAL Id: hal-02911834**

**<https://brgm.hal.science/hal-02911834v1>**

Submitted on 14 Feb 2022

**HAL** is a multi-disciplinary open access archive for the deposit and dissemination of scientific research documents, whether they are published or not. The documents may come from teaching and research institutions in France or abroad, or from public or private research centers.

L'archive ouverte pluridisciplinaire **HAL**, est destinée au dépôt et à la diffusion de documents scientifiques de niveau recherche, publiés ou non, émanant des établissements d'enseignement et de recherche français ou étrangers, des laboratoires publics ou privés.

1 **A new interpolation method to measure delta evolution and sediment flux:**  
2 **application to the late Holocene coastal plain of the Argens River in the western**  
3 **Mediterranean**

4

5 Jean-Philippe DEGEAI (1)\*, Frédérique BERTONCELLO (2), Matteo VACCHI (3, 4),  
6 Laurent AUGUSTIN (5), Alain DE MOYA (5), Luigi ARDITO (6), Benoît DEVILLERS (1)

7

8 (1) ASM UMR5140, Université Montpellier 3, CNRS, Ministère de la Culture, 34199  
9 Montpellier, France

10 (2) CEPAM UMR7264, Université Côte d'Azur, CNRS, 06357 Nice, France

11 (3) Dipartimento di Scienze della Terra, University of Pisa, Via Santa Maria 53, 56126  
12 Pisa, Italy

13 (4) CIRSEC, Center for Climate Change Impact, University of Pisa, Via del Borghetto 80,  
14 56124 Pisa, Italy

15 (5) DT INSU, C2FN, CNRS, 83507 La Seyne sur Mer, France

16 (6) BRGM, Centre scientifique et technique, 45060 Orléans, France

17

18

19 \*corresponding author

20 E-mail address: jean-philippe.degeai@cnrs.fr (J.-P. Degeai)

21

22

23 **ABSTRACT**

24 Rapid environmental changes along the Mediterranean coasts influenced the  
25 sedimentary dynamics, shoreline position and human settlements in deltaic areas over

26 the last millennia. An innovative and multiproxy approach using geostatistical modelling  
27 was developed to estimate geomorphic evolution and sediment fluxes in deltaic areas,  
28 while palaeoecological conditions and environmental changes were assessed from  
29 geochemistry and cluster analyses of molluscan fauna. This method was applied to the  
30 coastal plain of the Argens River (southern France) in the western Mediterranean. The  
31 study of facies associations led to the identification of depositional environments  
32 representative of prodelta, delta front, river channel, floodplain, marsh and abandoned  
33 channel. The late Holocene sediment flux in the Argens River bayhead delta ranged from  
34  $15,800 \pm 2300$  to  $52,000 + 8500 \text{ m}^3\cdot\text{yr}^{-1}$ . The highest rates of sediment deposition and  
35 delta growth occurred between 2500 and 2000 cal yr BP during a period of high flood  
36 frequency in the western Mediterranean. A geomorphically-induced decrease in  
37 subaqueous sediment flux over the past 2500 years and an increase in fluvial activity  
38 from 1600 to 500 cal yr BP were primarily controlled by autogenic processes due to  
39 change in accommodation space, delta slope and tributary junctions. A sharp increase in  
40 subaerial sediment flux from 500 to 0 cal yr BP was probably driven by hydroclimatic  
41 change characterized by more frequent flooding during the Little Ice Age. High sediment  
42 fluxes and climate-driven fluvial activity were associated with a southward shift of the  
43 North Atlantic westerlies or a northward migration of the intertropical convergence  
44 zone.

45

#### 46 KEYWORDS

47 Mediterranean delta; Coastal environment; Sediment flux; Elevation modelling;  
48 Inorganic geochemistry; Molluscan fauna; Late Holocene; Western Mediterranean

49

50

## 51 1. INTRODUCTION

52 In the western Mediterranean, the vulnerability of Holocene coastal landscape increased  
53 in response to rapid climate change characterized by pervasive millennial-scale  
54 variability as well as decadal- to centennial-scale abrupt transitions (Fletcher et al.,  
55 2013; Fletcher and Zielhofer, 2013; Melis et al., 2018). These rapid climate changes  
56 occurred during cooling events characterized by high storm activity and flood  
57 frequency, which led to an increased fluvial and coastal sediment supply (Dezileau et al.,  
58 2011, 2016; Sabatier et al., 2012; Fletcher and Zielhofer, 2013; Degeai et al., 2015,  
59 2017). These episodes of intense storm activity and high flood frequency could have  
60 been caused by changes in atmospheric circulation patterns such as the North Atlantic  
61 oscillation (NAO) or the intertropical convergence zone (ITCZ) (Benito et al., 2015a,  
62 2015b; Goudeau et al., 2015; Dezileau et al., 2016; Sanchez-Lopez et al., 2016; Degeai et  
63 al., 2017).

64 For instance, a southward shift of the North Atlantic westerlies and storm tracks related  
65 to the negative phase of the NAO was associated with cooler and wetter climatic  
66 conditions in southwestern Europe during the Little Ice Age (Nieto-Moreno et al., 2011,  
67 2013a, 2013b; Trouet et al., 2012; Wirth et al., 2013; Goudeau et al., 2014, 2015;  
68 Sanchez-Lopez et al., 2016). An increase in riverine flooding and fluvial activity occurred  
69 at this time (Macklin et al., 2006; Benito et al., 2015a; Degeai et al., 2017), which led to  
70 higher inputs of terrigenous material in the marine sediments of the western  
71 Mediterranean basin (Frigola et al., 2007; Nieto-Moreno et al., 2011, 2013a, 2013b;  
72 Goudeau et al., 2014, 2015; Jalali et al., 2016).

73 High fluvial sediment supply to coast and river mouths led to widespread coastal plains  
74 and an increased growth of bayhead deltas in incised-valley systems (Grove, 2001;  
75 Amorosi et al., 2009; Anthony et al., 2014). However, the quantitative impact of late

76 Holocene climate change on the sedimentation rates and fluvial activity of western  
77 Mediterranean deltas is poorly known, although these coastal areas are important to  
78 estimate sediment transport and flux from continent to ocean, or to assess the balance  
79 between onshore erosion and offshore deposition.

80 The evolution of deltas developed in western Mediterranean incised-valley systems was  
81 generally characterized by facies associations showing a succession of marine, lagoonal  
82 or fluvial conditions over the past millennia (Amorosi et al., 2009, 2013b, 2013c;  
83 Bertonecello et al., 2014a; Anthony, 2015). The identification of depositional  
84 environment and the study of sedimentary processes and palaeogeographic changes in  
85 the western Mediterranean delta plains during the Holocene were generally based on  
86 multiproxy analyses of sedimentary sequences from cores or trenches (e.g. Giraudi et al.,  
87 2009; Bertonecello et al., 2014a; Amorosi et al., 2016; Melis et al., 2018; Devillers et al.,  
88 2019; Ruiz-Pérez and Carmona, 2019). These methods are effective for coastal  
89 palaeoenvironmental reconstruction, but are often poorly suited to the geometric  
90 reconstruction of sedimentary units and the measurement of sediment volumes.

91 Geostatistics or numerical modelling were used to estimate palaeoelevation and  
92 sediment flux in coastal plains and incised-valley systems over the last millennia (e.g.  
93 Koster et al., 2017; Clement and Fuller, 2018). These interpolation methods are very  
94 useful in the case of limited age data and can provide important information on soil  
95 erosion, sediment flux, mass balance and geomorphic evolution in coastal areas.

96 In this paper, a new quantitative approach was developed to (1) calculate sediment flux  
97 associated with the progradation of bayhead deltas in incised-valley systems and (2)  
98 decipher the role of climate change and autogenic processes on delta growth. This new  
99 method was applied to the coastal plain of the Argens River in southeastern France,  
100 which is an area of particular interest for the study of atmospheric circulation patterns

101 between northern and southern Europe. The depositional environment and sedimentary  
102 dynamics over the past 2500 years were studied using an integrated methodology based  
103 on cores and archaeological excavations, sedimentological analyses (geochemistry,  
104 magnetic susceptibility), malacology and radiocarbon chronology, then geomorphic  
105 change and sediment flux were estimated from geostatistics and elevation modelling.  
106 The variability of sediment flux was discussed in relation to late Holocene hydroclimate  
107 change and geomorphic setting.

108

109

## 110 2. ENVIRONMENTAL SETTING

111 The Argens River drains a catchment of ca. 2800 km<sup>2</sup> located in southeastern France  
112 (Fig. 1A). This 114 km long river flows into the western Mediterranean between the Gulf  
113 of Lions and the Ligurian Sea along the southwestern Alps. This mountainous coastal  
114 area is bordered by a very narrow shelf (< 5 km) and a steep continental slope that  
115 stands above the floor of the Provençal Basin at depths greater than 2800 m. The source  
116 of the Argens River is at 268 m above sea level (Durozoy et al., 1970), giving an average  
117 slope of ca. 2.35‰ for the modern streambed. Over the last 50 years (1970-2019), the  
118 hydrological regime at Roquebrune-sur-Argens (Fig. 1B) was characterized by  
119 maximum and minimum river discharge rates in winter (32.2 m<sup>3</sup>.s<sup>-1</sup>) and summer (5.8  
120 m<sup>3</sup>.s<sup>-1</sup>), respectively, due to a Mediterranean rainfall regime (DREAL PACA data,  
121 [www.hydro.eaufrance.fr](http://www.hydro.eaufrance.fr)).

122 The lower valley of the Argens River is bounded on the south by the late Proterozoic to  
123 early Carboniferous granitic and gneissic rocks of the Massif des Maures (Fig. 1B), and  
124 on the north by the Permian volcano-sedimentary basin of the lower Argens valley  
125 (Toutin-Morin et al., 1994). At the end of the Last Glacial Maximum (LGM, ca. 20 cal kyr

126 BP), sea level dropped more than 100 m along the French Mediterranean coast  
127 (Lambeck and Bard, 2000), leading to an adjustment of the longitudinal profile of the  
128 river by regressive erosion (Bertoncello et al., 2014a). Thus, the lower valley of the  
129 Argens River was deeply incised in Lower Pliocene marine sediments composed of  
130 blueish or grey marl, sand and gravel (Toutin-Morin et al., 1994). This incised-valley  
131 system was then buried by transgressive deposits during the post-LGM sea level rise  
132 (Dubar, 2004).

133 In the lower valley, the post-LGM deposits form a >100 m thick sedimentary sequence  
134 composed of (1) fluvial sand and gravel at the bottom, (2) marine sand and clay  
135 intercalated with fluvial sand and gravel, and (3) fluvial silt, sand and gravel at the top  
136 (Durozoy et al., 1970; Toutin-Morin et al., 1994; Dubar, 2004). The latter deposits were  
137 formed by delta progradation and fluvial aggradation, which led to the formation of a  
138 coastal plain over the past 4000 years (Dubar, 2004; Bertoncello et al., 2014a). This  
139 coastal plain does not exceed 5 m in elevation over a distance of up to 5 km from the sea  
140 (Fig. 1B), giving a mean slope of 1‰.

141 Previous works studied the palaeogeographic and environmental changes in the Argens  
142 River coastal plain from the Neolithic to the Roman period and their impacts on human  
143 settlement (Dubar, 2004; Bertoncello et al. 2014a). The analyses of the palaeogeography  
144 at the mouth of the Argens River over the past three centuries from historical maps or  
145 archives highlighted a highly mobile coastal environment under the influence of the  
146 progradation of the Argens River along with its two main northern tributaries (i.e. the  
147 Garonne and Reyran rivers) and the southern branch of this delta system upstream from  
148 the Villepey Pond (Fig. 1B) (Cohen, 1997; Bertoncello et al., 2008, 2014a). In fact, these  
149 multiple channels formed a deltaic plain, hereafter called the Argens River delta system  
150 (ARDS).

151 The ARDS was classified as a bayhead delta that prograded into a protected bedrock  
152 embayment with low incident wave energy as a result of significant refraction,  
153 diffraction and nearshore dissipation (Anthony et al., 2014; Anthony, 2015). Bayhead  
154 deltas prograde in river-mouth setting along the inner part of wave-dominated estuaries  
155 (Dalrymple et al., 1992; Amorosi et al., 2005; Anthony et al., 2014), and become  
156 increasingly shaped by waves (Anthony, 2015). In the western Mediterranean, wave-  
157 dominated estuaries were filled with sediments during transgression then transformed  
158 into wave-dominated deltas during sea-level highstand (Amorosi and Milli, 2001; Milli et  
159 al., 2013). Confined or unconfined bayhead deltas are defined according to the geological  
160 and environmental setting: the former prograde into incised-valleys and their geometry  
161 is controlled by the morphology of the valley, while the latter prograde into open  
162 interdistributary bay and are a part of larger deltaic complexes (Simms and Rodriguez,  
163 2015; Simms et al., 2018). The ARDS bayhead delta is confined in the Argens River valley  
164 west of Fréjus, and unconfined in the interdistributary bay between Saint-Raphaël and  
165 Saint-Aygulf (Fig. 1B).

166 During the Late Holocene, or the Meghalayan (i.e. the last 4200 years b2k),  
167 palaeoenvironmental and palaeoecological studies showed that the progradation of the  
168 ARDS occurred in a marine depositional environment that gradually transformed into a  
169 delta plain during the late phases of sedimentary filling of the lower valley (Allinne et al.,  
170 2006; Devillers and Bonnet, 2006; Bertonecello et al., 2014a). Pollen data indicate that  
171 the first human impact on the landscape of the lower valley of the Argens River could  
172 have occurred around 7000 cal yr BP with indices of forest clearing and evidence of  
173 cereal cultivation during the late Neolithic period (Dubar et al., 2004; Bertonecello et al.,  
174 2014a). After ca. 3000 cal yr BP, human activities led to radical changes in the vegetation



175 cover, high forest clearing and metal pollution in the sediments of the ARDS (Dubar et  
176 al., 2004; Bertoncello et al., 2014a; Véron et al., 2018).

177 The past human occupation in the study area was more intense during the Roman  
178 period, especially from the creation of the Roman colony of *Forum Iulii* (Fréjus) (Fig. 1B)  
179 in the late first century BCE (Gascou, 1982; Gascou and Janon, 1985). The Roman  
180 harbour of *Forum Iulii* is now more than 1 km inland from the sea owing to the  
181 progradation of the ARDS during the last two thousand years (Excoffon et al., 2006,  
182 2010; Gébara and Morhange, 2010; Bertoncello et al., 2011; Bony et al., 2011; Giaime et  
183 al., 2019).

184

185

### 186 3. MATERIAL AND METHODS

#### 187 3.1. Cores and trenches

188 A geological database was created from sedimentary cores and archaeological trenches  
189 (Fig. 1B). It is based on published cores with geochronological and palaeoenvironmental  
190 data as well as on two new cores (BN1 and BN5) located in the downstream part of the  
191 ARDS. The 12-m long BN1 core (43°25'22"N, 6°44'02"E, 1.65 m in elevation) was  
192 sampled with a stationary piston corer. The 18.5-m long BN5 core (43°25'02"N,  
193 6°43'44"E, 1.67 m in elevation) was sampled with a stationary piston corer from 0 to 3  
194 m depth, a solid tube sampler equipped with a hydraulic hammer from 3 to 7 m depth,  
195 and a rotary drill auger from 7 to 18.5 m depth. The sediments at 3-4 m depth in the BN1  
196 core and at 3.4-4 and 5.63-6.75 m depth in the BN5 core were unsampled due to  
197 creeping and difficulty in coring layers with very coarse particles.

198

#### 199 3.2. Molluscan analysis

200 A volume of sediment of ca. 1000 cm<sup>3</sup> per sample was collected at an average interval of  
201 50 cm along the BN1 and BN5 cores for a malacological study. These samples were  
202 sieved using a 1 mm mesh (Sabatier et al., 2008, 2012; Dezileau et al., 2016). A total of  
203 2314 mollusc shells were identified and counted under stereomicroscope, representing  
204 85 species living in marine (44 species), brackish (7 species), freshwater (17 species) or  
205 terrestrial (17 species) environments. The mollusc species were assigned to ecological  
206 groups from previous work in the Argens River valley (Devillers and Bonnet, 2006) and  
207 from the World Register of Marine Species ([www.marinespecies.org](http://www.marinespecies.org)), the AnimalBase of  
208 the University of Göttingen ([www.animalbase.uni-goettingen.de](http://www.animalbase.uni-goettingen.de)) and the INPN database  
209 of the Museum National d'Histoire Naturelle ([inpn.mnhn.fr](http://inpn.mnhn.fr)).

210

### 211 3.3. Geochemistry

212 Geochemical analyses of sediments may provide information about the degree of salinity  
213 in subaqueous depositional environment from coastal or lacustrine areas: high (low)  
214 values of S, Cl and Sr can evidence brackish (freshwater) conditions (Lopez-Buendia et  
215 al., 1999; Chagué-Goff et al., 2002; Schofield et al., 2010; Moreno et al., 2012; Haenssler  
216 et al., 2013; Degeai et al. 2015, 2017). Moreover, the bulk of sulphur in coastal lakes can  
217 reflect the organic content of a sediment as a function of primary productivity in the  
218 water column (Striewski et al., 2009; Haenssler et al., 2013). High ratios of S/Cl may  
219 indicate organic-rich layers as S is high in organic-rich sediments (Croudace et al., 2006).  
220 Besides, an increase in Si, K and Rb is generally associated with riverine input in the  
221 western Mediterranean (Frigola et al., 2007; Martin-Puertas et al., 2010, 2011; Nieto-  
222 Moreno et al., 2011, 2013a; Rodrigo-Gamiz et al., 2011, 2014; Moreno et al., 2012;  
223 Martinez-Ruiz et al., 2015; Degeai et al., 2017). Elemental concentrations of coastal  
224 sediments from the western Mediterranean are usually normalized to Al to minimize

225 matrix effects (Dezileau et al., 2011, 2016; Sabatier et al., 2012). Therefore, we have  
226 used the Cl/Al and Sr/Al ratios as paleosalinity indicators, the Si/Al, K/Al and Rb/Al  
227 ratios as proxy records of riverine input, and the S/Cl ratio as an indicator of organic  
228 matter content.

229 A total of 108 and 138 sediment samples from the BN1 and BN5 cores, respectively,  
230 were measured by energy-dispersive X-ray fluorescence (ED-XRF) spectrometry at an  
231 average sampling interval of ca. 10 cm with a Delta Innov-X spectrometer equipped with  
232 a 4 W Au-tube. Each sample was dried then mechanically crushed and homogenized to a  
233 fine powder, which was placed in a crystal polystyrene tube of 22 mm length and inner  
234 diameter then covered with an ultrafine polyethylene film. The measurement of S, Cl, Rb  
235 and Sr was undertaken with the soil analytical mode, while Al, Si and K were measured  
236 with the mining analytical mode. The parameters of voltage, amperage and counting  
237 times were as follows: 10 kV, 200  $\mu$ A and 10 s for Al, Si and K; 15 kV, 200  $\mu$ A and 45 s for  
238 S and Cl; 40 kV, 100  $\mu$ A and 30 s for Rb and Sr. The elemental concentrations were  
239 obtained using the Compton Normalization calibration method (EPA, 2007). The 2- $\sigma$   
240 measurement uncertainty is lower than  $\pm$  5% for Si, K, Rb and Sr, and around  $\pm$  10% for  
241 S and Cl.

242

### 243 3.4. Magnetic susceptibility

244 In deltaic environment, the magnetic susceptibility can reflect the terrigenous flux  
245 derived from fluvial processes (Delile et al., 2015). Higher values of magnetic  
246 susceptibility are generally driven by the presence of Fe-bearing minerals (e.g. biotite)  
247 in the sample (Dearing, 1999).

248 The mass-specific magnetic susceptibility ( $\chi$ ) of sediments from the BN1 and BN5 cores  
249 was measured at an average sampling interval of ca. 10 cm with a Bartington MS2

250 susceptibilimeter and a MS2B probe. Each powder sample in the tubes used for  
251 geochemical analyses (i.e. 246 samples for BN1 and BN5) was weighed then measured  
252 twice with a time period of 12s, an operating frequency of 4.65 kHz, an amplitude of  
253 applied magnetic field of 250  $\mu\text{T}$ , and a resolution of  $1 \times 10^{-8} \text{ kg.m}^{-3}$  (range 0.1). The  
254 relative standard deviation of both measurements is systematically lower than 3%.

255

### 256 3.5. Geochronology

257 The geochronological data are based on a compilation of available radiocarbon ages in  
258 the ARDS, including a set of 10 new Accelerator Mass Spectrometry (AMS)  $^{14}\text{C}$  dates on  
259 wood and charcoal from the BN1 and BN5 cores (Table 1). The new AMS  $^{14}\text{C}$  ages were  
260 performed by the Centre de Datation par le RadioCarbone at Lyon and by the Poznan  
261 Radiocarbon Laboratory. The Calib 7.10 software (Stuiver et al., 2019) was used to  
262 calibrate the new  $^{14}\text{C}$  dates and to update the calibration of radiocarbon ages published  
263 in previous studies. The radiocarbon ages of terrestrial material (seed, wood, charcoal,  
264 peat) were calibrated using the IntCal13 calibration curve (Reimer et al., 2013), while  
265 the radiocarbon ages of marine shell were calibrated using the MARINE13 calibration  
266 curve (Reimer et al., 2013) and a  $\Delta R$  of -15 years (Siani et al., 2000). The 2- $\sigma$  uncertainty  
267 interval and median probability of calibrated ages are reported in Table 1.

268

### 269 3.6. Geostatistics

270 Three 2D age-elevation transects (A1-3, see location in Fig. 1B) and five maps of  
271 sediment thickness in the ARDS were computed for the last 2500 years using the ArcGIS  
272 10 Geostatistical Analyst extension. The geochronological and sediment thickness data  
273 were interpolated using radial basis functions. The computation of rasters of sediment  
274 thickness with a spatial cell of 15 m in size for each 500-year interval over the past 2500

275 years was based on the isochrones of the 2D age-elevation models and on a null  
276 thickness assigned to the boundary of Holocene deposits. The models were limited to  
277 the last 2500 years because there are not enough  $^{14}\text{C}$  dates without age reversals to  
278 make a robust data interpolation before 2500 cal yr BP (Table 1).  
279 The palaeoelevation  $Z_n$  was then calculated at a 500-year interval from  $n = 1$  (500 cal yr  
280 BP) to 5 (2500 cal yr BP) using the ArcGIS 10 raster calculator and equation [1]. For  
281 spatial coordinates  $(x, y)$ ,  $Z_n$  was obtained by subtracting the cumulative sediment  
282 thickness  $T$  from the modern elevation  $Z_0$ , which is deduced from LiDAR data available  
283 for the ARDS (Litto3D, IGN/SHOM, year 2015), and by adding the sea level  $S_n$  at the time  
284  $n$  from Vacchi et al. (2016).

285

$$286 \quad Z_n(x, y) = Z_0(x, y) - \sum_{i=1}^n T_i(x, y) + S_n \quad [1]$$

287

288 Error estimates for sediment thickness and palaeoelevation were calculated with an  
289 uncertainty of  $\pm 100$  years for the isochrones of the 2D age-elevation models. This 200-  
290 year interval was chosen because it closely matches the mean 2- $\sigma$  uncertainty interval  
291 (225 years) of calibrated radiocarbon ages (Table 1).

292

293

## 294 4. RESULTS

### 295 4.1. Lithology

296 Both BN1 and BN5 cores were divided into 4 stratigraphic units from bottom (unit 1) to  
297 top (unit 4) (Fig. 2, 3).

298 Unit 1 in BN1 core (12-9 m depth) is characterized by alternating 10-20 cm thick layers  
299 of grey to greyish brown clay, silt and fine sand (Fig. 2). Moreover, particulate organic

300 matter is abundantly present in the matrix of sediments deposited from 11.8 to 10.2 m  
301 depth. In BN5 core, unit 1 (18.5-11.4 m depth) is primarily composed of grey clay and  
302 silty clay alternating with grey clayey silty fine sand at ca. 16 and 14.1-13.4 m depth,  
303 with brownish grey sand at ca. 18.4, 17.5, 16.8 and 16.4 m depth, and with grey sand and  
304 gravel at 16.5 and 12.7-12 m depth (Fig. 3). The clay content decreases above 14.85 m  
305 depth.

306 Unit 2 in BN1 core (9-4 m depth) is mainly composed of grey, greyish brown, brownish  
307 grey or brown sand interbedded with silt and sandy silt (Fig. 2). The upper part shows a  
308 coarsening-upward trend from silt to medium-coarse sand. Thin organic-rich layers can  
309 be observed at 8.7-8.6, 8.25-8, 6.3-6.1 and 5.3-5.2 m depth, while charcoals are present  
310 around 5.7 m depth. In BN5 core, unit 2 (11.4-6.75 m depth) exhibits a succession of  
311 grey sediments characterized by a general coarsening-upward trend showing fine sandy  
312 silt and silty fine sand overlaid with fine sand from 8.5 to 8.1 m depth then with clayey  
313 medium-coarse sand and rounded gravel from 8.1 to 7.3 m depth. Particulate organic  
314 matter appears at ca. 11.3-11.2, 9.6-9.4 and 8.7-8.5 m depth (Fig. 3). The top of unit 2 in  
315 BN5 core is composed of organic-rich grey clay between 7.3 and 6.75 m depth with black  
316 peat from ca. 7 to 7.2 m depth. This layer is absent in BN1.

317 Unit 3 in BN1 core (3-1.4 m depth) is represented by brown sand and clast-supported  
318 rounded gravel showing a general upward-finishing trend with fine-medium sand  
319 overlying coarse sand and gravel (Fig. 2). In BN5 core, the coarse sand and clast-  
320 supported rounded gravel of unit 3 (5.63-4 and 3.4-2.9 m depth) have a brownish grey  
321 or greyish brown colour in the lower part and a brown colour above 4.85 m depth (Fig.  
322 3). The bottom of this unit is uncertain in BN5 core given the coring gap from 6.75 to  
323 5.63 m depth.

324 Unit 4 in BN1 core (1.4-0 m depth) is composed of brown clay, silt and fine sand with  
325 many rootlets and of a 20 cm thick dark brown clayey layer at the bottom (Fig. 2). In  
326 BN5, unit 4 (2.9-0 m depth) is mainly composed of brownish grey or greyish brown fine  
327 sand interbedded with thin layers of clay and silty clay between 2.9 and 2.2 m depth, of  
328 greyish brown clay between 2.2 and 1.5 m depth, and of brown silt, clayey silt or fine  
329 sand between 1.5 and 0 m depth (Fig. 3). Small fragments of modern ceramics and a 15  
330 cm thick layer of dark brown silt and matrix-supported angular or rounded gravel  
331 overlaid with a 4 cm thick layer of black organic silt appear in the upper 40 cm of BN5  
332 core. Unit 4 in BN5 core contains particulate organic matter, rootlets and charcoals.  
333 Overall, bedding contacts are gradual apart from sand layers which are generally in  
334 sharp contact with clay or silt beds. Marine, brackish, freshwater gastropods and  
335 bivalves are present in units 1 and 2, while terrestrial gastropods are over-represented  
336 in unit 4. Unit 3 is barren of fossils.

337

#### 338 4.2. Molluscan shells

339 The palaeoecological conditions prevailing in the BN1 and BN5 cores were deduced  
340 from a multivariate cluster analysis of molluscan assemblages (Fig. 4, 5).

341 Unit 1 is characterized by a salinity-stressed marine environment with low to moderate  
342 brackish and freshwater influences. The dominant species of this ecosystem correspond  
343 to *Turbonilla lactea* for BN1 (41% on average) and to *Moerella donacina* for BN5 (19%  
344 on average). Subordinate marine species (1-10% on average) are represented by *Abra*  
345 *prismatica*, *Corbula gibba*, *Eulima bivittata*, *Macomangulus tenuis*, *Smaragdia viridis*,  
346 *Thracia pubescens*, *Trivia arctica* and *Trophonopsis muricata* for BN1, and by *A.*  
347 *prismatica*, *Acanthocardia* sp., *Antalis dentalis*, *C. gibba*, *Gouldia minima*, *Lentidium*  
348 *mediterraneum*, *M. tenuis*, *Mathilda quadricarinata*, *Megastomia conoidea*, *Mimachlamys*

349 *varia*, *Nucula nucleus*, *Saccella commutata* and *Venus verrucosa* for BN5. A low to  
350 moderate mean abundance (1-12% in BN1 or BN5) of molluscs such as *Abra alba*,  
351 *Cerastoderma glaucum*, *Hydrobia acuta*, *Loripes orbiculatus*, *Parvicardium exiguum*,  
352 *Ancylus fluviatilis*, *Bithynia tentaculata*, *Islamia spirata* and *Valvata* sp. suggests that the  
353 marine environment experienced brackish and freshwater conditions with fluvial  
354 discharges.

355 Unit 2 is characterized by brackish and freshwater environmental conditions with  
356 marine influences (Fig. 4, 5). The molluscan assemblages are predominantly composed  
357 of *A. Alba*, *C. glaucum*, *H. acuta* and *Valvata* sp. (> 10% on average in BN1 or BN5). Other  
358 subordinate brackish or freshwater species in BN1 or BN5 include *A. fluviatilis*,  
359 *Belgrandia gibba*, *B. tentaculata*, *Euglesa casertana*, *I. spirata* and *Theodoxus fluviatilis*  
360 (1-10% on average). The rare occurrence (< 1%) of terrestrial molluscs usually found in  
361 sandy dunes such as *Cerneuella virgata*, *Cochlicella conoidea*, *Trochoidea trochoides* and  
362 *Xerosecta explanata* suggests reworking of coastal sediment, while a low to moderate  
363 mean abundance (1-12% in BN1 or BN5) of *Abra nitida*, *A. prismatica*, *C. gibba*, *L.*  
364 *mediterraneum*, *Lucinella divaricata*, *M. donacina*, *N. nucleus*, *Retusa umbilicata*, and *T.*  
365 *lactea* highlight marine influences.

366 Unit 3 is barren of molluscan shells, whereas unit 4 is characterized by a terrestrial  
367 environment with low to moderate humid conditions (Fig. 4, 5). The most abundant land  
368 snails are represented in BN1 and BN5 by species living in dry habitats of coastal areas  
369 like sandy dunes or beaches: *C. virgata* (45 and 30% on average, respectively) and *C.*  
370 *conoidea* (7 and 43% on average, respectively). The most frequent subordinate  
371 terrestrial species (1-10% on average) correspond to gastropods living in dry vegetation  
372 or on sandy dunes in coastal areas (*Cochlicella acuta*, *Trochoidea pyramidata*, *T.*  
373 *trochoides*, *X. explanata*). Other uncommon land molluscs (< 6% on average) live in



374 either humid habitats (*Cecilioides acicula*, *Oxychilus draparnaudi*, *Oxyloma elegans*,  
375 *Vallonia pulchella*) or open habitats with very variable humidity (*Vertigo pygmaea*). The  
376 main species of freshwater molluscs are *B. tentaculata*, *Galba truncatula*, *I. spirata*,  
377 *Musculium lacustre* and *Valvata* sp. (1-10% on average). A rare occurrence (< 3%) of *H.*  
378 *acuta* is found between 1.5 and 1 m depth in BN1, while the absence of marine shells is  
379 observed in both BN1 and BN5 cores.

380

#### 381 4.3. Geochemical data

382 Unit 1 generally exhibits high values of Cl/Al and Sr/Al, which reflect high levels of  
383 salinity (Fig. 2, 3). However, higher than average riverine inputs (K/Al and Rb/Al but not  
384 Si/Al) accompanied with lower values of Cl/Al and Sr/Al at the bottom of BN1 and BN5  
385 cores could reveal fluvial influence in a marine depositional environment. The layers of  
386 brownish grey sand or grey sand and gravel in unit 1 of BN5 are associated with peaks  
387 of Si along with low levels of salinity (Fig. 3). These coarse sediments could reflect local  
388 and brief episodes of high-energy fluvial input. The high content of S at the transition  
389 between units 1 and 2 from 9.3 to 8.1 m depth in BN1 is associated with abundant  
390 tabular crystals of euhedral gypsum in the sand fraction (Fig. 2).

391 Unit 2 is characterized by a general decrease of salinity indicators paralleled by an  
392 increase in riverine input indicators (Fig. 2, 3). The values of elemental ratios in the  
393 upper part of unit 2 show low levels of salinity and high riverine input in both BN1 and  
394 BN5 cores. In this latter, the organic-rich clayey layer at the top of unit 2 exhibits high  
395 ratios of K/Al, Rb/Al and S/Cl, while the highest concentration of S is found in the black  
396 peat horizon between ca. 7.2 to 7 m depth.

397 Unit 3 presents geochemical and sedimentological features characterized by high Si/Al  
398 and K/Al ratios, low salinity indices, and coarse sand and gravel most likely deposited in  
399 high-energy environment (Fig. 2, 3).

400 Unit 4 in BN1 core shows higher than average riverine discharge and very low levels of  
401 salinity (Fig. 2). Large peaks of K/Al and Rb/Al are associated with a 20 cm thick layer of  
402 dark brown clayey sediment at the bottom of this unit. Besides, a major peak of S/Cl is  
403 found at the transition between units 3 and 4 in BN1 core, and is perhaps indicative of  
404 higher organic matter content. In BN5 core, the lower half of unit 4 between 2.9 and 1.55  
405 m depth generally shows higher than average Rb/Al and K/Al ratios, low Si/Al ratio, and  
406 peaks of Sr/Al, whereas lower than average indicators of riverine input and salinity are  
407 most often found in the upper half of this unit above 1.55 m depth (Fig. 3).

408 Overall, high (low) levels of salinity in both BN1 and BN5 cores generally correspond to  
409 low (high) levels of riverine input. Hence, the variability of salinity indicators in the  
410 ARDS could have been mainly driven by fluvial activity. Besides, the geochemical  
411 indicators of riverine discharge seem to have been influenced by the grain size of  
412 sediments. High values of Si/Al are found only in sand and gravel, and more specifically  
413 in the coarse sand and gravel fraction (Fig. 2, 3). High values of Rb/Al are observed only  
414 in clay and silt, while high values of K/Al can be recorded in coarse or fine sediments. K  
415 and Rb are commonly associated with detrital clay (Croudace et al., 2006). However, the  
416 K/Al ratio is also influenced by the contribution of detrital K-feldspar, which may be  
417 significant in the coarse fraction (Martinez Ruiz et al., 2015).

418

#### 419 4.4. Magnetic susceptibility

420 The values of mass-specific magnetic susceptibility ( $\chi$ ) are generally lower than  $10 \times 10^{-8}$   
421  $\text{m}^3 \cdot \text{kg}^{-1}$  in BN1 and BN5 (Fig. 2, 3). Higher than average  $\chi$  values are found in the basal

422 part of both cores (unit 1) from 12 to ca. 10 m depth in BN1 and from 18.5 to 16.9 m  
423 depth in BN5.  $\chi$  values ranging between ca. 10 and  $20 \times 10^{-8} \text{ m}^{-3} \cdot \text{kg}^{-1}$  appear from 5.8 to  
424 4.5 m depth in unit 2 of BN1 and from 3.3 to 2 m depth at the transition between units 3  
425 and 4 in BN5. The highest  $\chi$  values around  $30 \times 10^{-8} \text{ m}^{-3} \cdot \text{kg}^{-1}$  are found at the top of BN1  
426 and BN5 cores.

427 Higher  $\chi$  values in deltaic environment should reflect a terrigenous supply from  
428 catchment by fluvial processes (Delile et al., 2015). However, the riverine sediments of  
429 unit 3 are characterized by low  $\chi$  values (Fig. 2, 3). In fact, the mineralogical composition  
430 of coarse sand and gravel can preclude the use of magnetic susceptibility as a reliable  
431 proxy record of fluvial activity. The low  $\chi$  values of sediments from unit 3 suggest that  
432 these coarse alluvial deposits are mainly composed of diamagnetic material such as  
433 quartz (Dearing, 1999). High values of Si and Si/Al as in unit 3 can be indicative of high  
434 relative content of quartz (Martinez-Ruiz et al., 2015). This is confirmed by  
435 stereomicroscopic observations, which show that the alluvial deposits of unit 3 exhibit  
436 an important content of quartz for particles coarser than 1 mm.

437 By contrast, the high  $\chi$  values of the fine sediments in the upper 1.5 m of BN5 are not  
438 related to high values of elemental ratios indicative of riverine input. In fact, this  
439 increase in magnetic susceptibility could have been caused by post-depositional  
440 oxidation and weathering of sediments at the top of the BN5 core, which is characterized  
441 by a terrestrial environment as evidenced by molluscan fauna (Fig. 3, 5).

442

443

#### 444 5. PALAEOENVIRONMENTAL INTERPRETATION

445 Delta systems in the northwestern Mediterranean are often characterized by a vertical  
446 stacking of mid-late Holocene prodelta, delta front and delta plain deposits (Dubar and

447 Anthony, 1995; Amorosi et al., 2008, 2013c). These deltaic sequences are interpreted as  
448 highstand systems tracts deposited during the deceleration of sea level rise after 7500  
449 cal yr BP (Stanley and Warne, 1994; Somoza et al., 1997; Vacchi et al., 2016).

450 The depositional environments of the BN1 and BN5 sedimentary successions can be  
451 defined on the basis of a comparison of molluscan assemblages, lithology, sediment  
452 properties and geochemical data (Fig. 2-5) with facies associations described for the  
453 northwestern Mediterranean deltas of (1) the Argens River (Allinne et al., 2006;  
454 Devillers and Bonnet, 2006; Bertoncetto et al., 2014a), Hérault River (Devillers et al.,  
455 2019), Rhône River (Amorosi et al., 2013c) and Var River (Dubar and Anthony, 1995) in  
456 southern France, (2) the Arno River (Amorosi et al., 2009, 2013a, 2013b), Biferno River  
457 (Amorosi et al., 2016), Po River (Amorosi et al., 2008), Posada River (Melis et al., 2018)  
458 and Tiber River (Giraudi et al., 2009) in Italy, and (3) the Ebro River (Somoza et al.,  
459 1997) and Turia River (Ruiz-Pérez and Carmona, 2019) in eastern Spain (Fig. 1A).

460 Holocene prodeltas in the northwestern Mediterranean are characterized by (1)  
461 salinity-stressed and strongly fluvial-influenced marine environment with abundant  
462 marine gastropods and mixed brackish-normal saline conditions, and (2) clay-sand  
463 alternations showing an upward decrease in clay content accompanied with an increase  
464 in the frequency and thickness of sandy layers (Somoza et al., 1997; Amorosi et al., 2008,  
465 2009, 2013b, 2013c). In both BN1 and BN5 cores, unit 1 is mostly composed of grey to  
466 brownish grey clay and silty clay with intercalations of sand layers deposited in a  
467 marine environment with high levels of salinity (Fig. 2, 3). From the bottom to the top of  
468 unit 1, the sandy layers are thicker or more frequent and clay content decreases. In BN5  
469 core, the presence of massive mud below 17 m depth and the increasing sand content  
470 above this depth fit well with the bottom sediment distribution of the modern inner  
471 shelf environment along the ARDS, which shows a minimum upper limit of onshore

472 blue-grey mud and a minimum lower limit of nearshore terrigenous sand at ca. 15 m  
473 below sea level (Toutin-Morin et al., 1994). The abundance of marine molluscs ranges  
474 from ca. 45 to 75% in BN1 core and from ca. 50 to 95% in BN5 core. Moreover, riverine  
475 inputs highlight a marine environment with fluvial influence. Hence, unit 1 is defined as  
476 a prodelta.

477 In the northwestern Mediterranean, the sedimentary features associated with the  
478 transition from prodelta to delta front typically exhibits an increasing proportion of  
479 sand, with a delta front composed of an upward-coarsening sand body deposited in  
480 high-energy environment (Somoza et al., 1997; Amorosi et al., 2008, 2013c). The lower  
481 and middle parts of unit 2 in BN1 and BN5 cores are characterized by many layers of  
482 sandy silt or fine sand, while the upper part shows upward-coarsening sand bodies in  
483 which the sand fraction changes from fine sand to medium-coarse sand from bottom to  
484 top (Fig. 2, 3). Unit 2 is also characterized by a decrease in marine shells (from ca. 50 to  
485 0%) paralleled by a decrease in Cl/Al and an increase of riverine input (Fig. 2, 3). This  
486 unit can be considered as a ca. 5 m thick delta front, which is consistent with the delta  
487 front thickness of 5.5 and 7 m in PL1 and PAL1 cores, respectively (Fig. 6). In BN5 core,  
488 the delta front is overlaid with organic-rich sediments and black peat, which were likely  
489 deposited in a marsh environment (Fig. 3).

490 The sediments of unit 3 are composed of poorly sorted coarse sand and clast-supported  
491 gravel devoid of fossils (Fig. 2, 3). Fining-upward trends are found in unit 3 at BN1 and  
492 from the top of unit 3 to the lower half of unit 4 at BN5. These sedimentological and  
493 biological features are typical of high-energy environments such as fluvial channels  
494 (Dubar and Anthony, 1995; Somoza et al., 1997; Amorosi et al., 2009, 2013a, 2013b,  
495 2013c, 2016; Giraudi et al., 2009; Melis et al., 2018; Devillers et al., 2019; Ruiz-Pérez and  
496 Carmona, 2019). Moreover, a deposition of the coarse sediments of unit 3 in a river

497 channel is consistent with the geochemical data, which show very low levels of salinity  
498 and high values of Si/Al and K/Al indicative of riverine input.

499 Unit 4 in BN1 core and the upper half of unit 4 in BN5 core are mainly composed of  
500 bioturbated brown clay, silt and fine sand with land molluscs and very low levels of  
501 salinity (Fig. 2, 3). These sedimentological and palaeoecological features are compatible  
502 with a depositional environment in a well-drained floodplain occasionally affected by  
503 river floods (Somoza et al., 1997; Allinne et al., 2006; Devillers and Bonnet, 2006;  
504 Amorosi et al., 2013a, 2016; Bertonecello et al., 2014a; Melis et al., 2018; Devillers et al.,  
505 2019; Ruiz-Pérez and Carmona, 2019). The delta plain of the ARDS includes both  
506 floodplain and river channels. More specifically, the malacological data point to a delta  
507 plain environment subject to subaerial exposure, given the high abundance of terrestrial  
508 species living in coastal habitats such as *Cerneuella virgata*, *Cochlicella conoidea*,  
509 *Trochoidea trochoides* and *Xerosecta explanata* at the top of BN1 and BN5 cores (Fig. 4,  
510 5). Land snails and freshwater molluscs associated with humid or aquatic environment  
511 are mostly found in the lower part of unit 4 and are probably indicative of a depositional  
512 setting more frequently subjected to riverine flooding or hydromorphic conditions.

513 In the lower half of unit 4 in BN5 core, thin layers of brownish grey to greyish brown  
514 sand and silt (ca. 2.9-2.2 m depth) then organic-rich greyish brown massive clay with  
515 rootlets at the top (ca. 2.2-1.5 m depth) were deposited on the coarse fluvial sediments  
516 of unit 3 (Fig. 3). These sediment properties and the stratigraphic relationship with  
517 fluvial-channel sediments are typical of alluvial sub-environments close to river channel  
518 (Amorosi et al., 2013a, 2016). Besides, the organic-rich sediments of the lower half of  
519 unit 4 in BN5 core show a general fining-upward trend such as in abandoned channel  
520 fills, which are characterized by an initial proximal fill during the abandonment stage  
521 then by a distal fill collected in the abandoned palaeochannel during the disconnected

522 stage (Toonen et al., 2012). These two stages of channel-fill development could explain  
523 the sediment deposition at ca. 2.9-2.2 and 2.2-1.5 m depth, respectively, in BN5 core.  
524 Higher than average values of Sr and Sr/Al are recorded in the lower half of unit 4 in  
525 BN5 core and could be due to episodes of shallowing and salinization of water bodies in  
526 an abandoned fluvial channel, for example during hydroclimatic changes. Indeed,  
527 enhanced Sr may indicate the presence of high-Sr aragonite which requires a shallow-  
528 water source (Croudace et al., 2006). Besides, higher Sr/Al ratios were recorded by  
529 Holocene lacustrine deposits in the western Mediterranean during periods of evaporite  
530 precipitation due to lower lake levels characterized by Sr-rich sediments (Martin-  
531 Puertas et al., 2011).

532

533

## 534 6. NUMERICAL MODELLING

### 535 6.1. 2D age-elevation models

536 An accurate chronology of deltaic sequences can be difficult to determine because of  $^{14}\text{C}$   
537 age reversals due to sediment storage and remobilization of older deposits during  
538 downslope alluvial transport that prevails in fluvial and delta plains (Stanley and Hait,  
539 2000; Stanley, 2001).

540 The median probability of 10 new radiocarbon dates obtained for the BN1 and BN5  
541 cores ranges from 3565 to 440 cal yr BP (Table 1). However, the 4 radiocarbon ages of  
542 charcoals and wood sampled in delta front deposits are too old and show a reversal of  
543 the median probability (Fig. 2, 3). This seems to indicate that reworking of older  
544 terrestrial organic matter from the catchment was more important in the delta front  
545 depositional environment. By excluding these 4 radiocarbon ages, the sediments from

546 the BN1 and BN5 cores would have been deposited approximately during the last 2500  
547 years.

548 Amongst the 41 radiocarbon dates compiled in the ARDS, we discarded 12 dates (ca.  
549 30% of total) showing age reversals with a median probability older than expected  
550 (Table 1). These reversal patterns are probably due to the remobilization and  
551 redeposition of older material (Stanley and Hait, 2000; Stanley, 2001). The cores from  
552 the ancient harbour of *Forum Iulii* (FIX, FXI, SC6) (Fig. 1B) were not used owing to  
553 potential sedimentary hiatuses caused by possible dredging in this port basin during the  
554 Roman period (Bony et al., 2011). Besides, several  $^{14}\text{C}$  dates from the PL1 core exhibit  
555 large  $2\text{-}\sigma$  uncertainty intervals higher than 300 years because of a very large plateau of  
556 the calibration curve from ca. 800 to 400 cal yr BCE (i.e. a conventional  $^{14}\text{C}$  age around  
557 2450 BP), the so-called Hallstatt plateau (Fontugne, 2004; Van der Plicht, 2004). Finally,  
558 a total of 29 radiocarbon ages were used to compute three 2D age-elevation models in  
559 the ARDS: one longitudinal age profile (A1) and two transverse age profiles (A2 and A3)  
560 across the valley (Fig. 6). The isochrones are displayed with a 100-year resolution.

561 Overall, profile A1 shows a downstream thickening of deposits from PL1 to BN5 over the  
562 last 2500 years. The thickest part is located between PAL1 and BN5 where a mean  
563 sediment thickness of ca. 18 m was deposited during the last 2500 years. The highest  
564 accumulation occurred between 2500 and 2000 cal yr BP in this part of profile A1.

565 Profile A2 and the northwestern part of profile A1 exhibit a lower sediment  
566 accumulation with a thickness of ca. 5 m upstream of the ARDS during the last 2500  
567 years. Profile A3 shows that the sediments deposited downstream of the coastal plain  
568 over the past 2500 years are thicker in the central part of the valley around BN5 and  
569 thinner on the southern edge of the ARDS, with a thickness of ca. 7 m in the VIL2 core  
570 (Fig. 6). On the northern side, the trench dug during the Théâtre d'agglomération T2



571 (TAT2) archaeological excavation revealed that Permian rocks were buried under  
572 coastal sediments during the second half of the first century BCE (Excoffon et al., 2006;  
573 Devillers et al., 2007). These Permian rocks were then covered by 2-3 m of sediments  
574 over the last 2000 years.

575 Although the lack of chronological data in the easternmost part of the ARDS coastal plain  
576 does not allow the age models to be robustly estimated in this area, LiDAR data were  
577 shifted along the BN5 age-elevation model in order to propose a hypothetical  
578 reconstruction of the isochrones of the unconfined bayhead delta that prograded onto  
579 the inner shelf (Fig. 6). The depositional architecture and stacking pattern east of BN5  
580 are thus very similar to those of steep-face deltas studied by Dubar and Anthony (1995)  
581 along the southern French Alps, such as the Var River delta located at ca. 70 km  
582 northeast of the Argens River (Fig. 1A).

583

## 584 6.2. Sediment thickness

585 The numerical models of sediment thickness of the Argens River bayhead delta cover an  
586 area of 12.2 km<sup>2</sup> (Fig. 7). These spatial models were focused on the incised-valley system  
587 west of Fréjus, in which the eastward progradation of the bayhead delta of the Argens  
588 River was confined and controlled by the morphology of the valley. Moreover, the lack of  
589 data in the easternmost part of the ARDS coastal plain prevents the models to be  
590 extended east of Fréjus. Therefore, the eastern limit of the modelled area corresponds  
591 approximately to the eastern boundary of the Argens River valley between Fréjus and  
592 the eastern side of the Massif des Maures.

593 The thickness of sediments deposited from 2500 to 2000 cal yr BP ranges from < 1 to 8  
594 m in the study area, with maximum values around the PAL1 site (Fig. 7A). The  
595 depocenter was located in the central part of the lower valley of the Argens River. From

596 2000 to 1500 cal yr BP, the depocenter moved downstream in an eastward direction  
597 (Fig. 7B). The main depositional area was located between BN5 and BN1, with a  
598 maximal thickness of deposits estimated between 4 and 5 m. Another area of moderate  
599 accumulation ranging from 1 to 3 m in thickness can be observed along a northwest-  
600 southeast direction of the valley from PL1 to PAL1.

601 After 1500 cal yr BP, the maximum accumulation of sediments was lower than 4 m for  
602 each 500-year period and the depocenter stayed close to the modern mouth of the  
603 Argens River (Fig. 7C-E). The depocenter moved southward from 1500 to 1000 cal yr BP  
604 and shows a maximum thickness of 3-4 m at BN5 (Fig. 7C). The sediment thickness  
605 pattern between 1000 and 500 cal yr BP was quite similar to the previous period, with  
606 maximum values of 2-3 m (Fig. 7D). From 500 to 0 cal yr BP, the highest sediment  
607 accumulation occurred in two areas located, on the one hand, between Verteil and ESC1,  
608 and, on the other hand, close to the mouth of the Argens River around BN5 (Fig. 7E).

609

### 610 6.3. Elevation modelling and coastal palaeogeography

611 Deltaic areas with elevation above or below sea level correspond to subaerial or  
612 subaqueous delta, respectively (Anthony, 2015). The past sea levels are taken from  
613 Vacchi et al. (2016) (Table 2).

614 At 2500 cal yr BP, the elevation model reveals that the lower valley of the Argens River  
615 was largely occupied by a marine bay with a subaqueous delta extended until the Verteil  
616 site and a prodelta/delta front transition located between PL1 and PAL1 (Fig. 8A). The  
617 reduction in the surface area of the subaqueous delta between 2500 and 2000 cal yr BP  
618 was probably due to the progradation of the Argens, Reyran and Garonne rivers, which  
619 would have led to an eastward displacement of the prodelta/delta front transition  
620 between PAL1 and BN5 and to a decrease of the maximum depth of the marine bay from

621 ca. 15 to 10 m (Fig. 8A-B). Then the transition between the delta front and the prodelta  
622 moved east of BN5 after 2000 cal yr BP (Fig. 8B-C).

623 During the first millennium CE, elevation models suggest that land emergence seems to  
624 have been more important in the northern part of the ARDS, while subaqueous delta  
625 environment would have persisted on the southern side of the ARDS between PAL1,  
626 BN5 and VIL2 at the same time (Fig. 8B-D). The progradation in the southern part of the  
627 ARDS occurred mainly during the last millennium and would have been characterized by  
628 the formation of a fan-delta that grew between BN5 and VIL2 (Fig. 8D-E). Historical  
629 maps show that the downstream flow of the Argens River was divided into two branches  
630 at least from the end of the 16th century CE to the end of the 18th century CE (Cohen,  
631 1997; Bertonecello et al., 2008, 2014a). In addition to the southern branch of the Argens  
632 River, the Villepey River might also have contributed to the progradation in the southern  
633 part of the delta system, as shown by maps from the 18th century CE (Bertonecello et al.,  
634 2008, 2014a).

635 The transition from subaqueous to subaerial delta at PAL1 and BN1 occurred between  
636 1000 and 500 cal yr BP. At 500 cal yr BP, the elevation model suggests that a large part  
637 of the delta plain was above sea level, while a shallow body of water (< 1 m depth)  
638 oriented in a NNE-SSW direction persisted along the coastline (Fig. 8E). Moreover, a  
639 seaward progradation of ca. 1 km on average should have occurred between BN5 and  
640 VIL2 during the last 500 years, which yields a mean progradation rate of 2 m.yr<sup>-1</sup>.

641 The present topography of the coastal plain exhibits an area of lower elevation between  
642 ESC1 and PL1 around the Garonne River, which is surrounded by two levees along the  
643 Reyran River north of PAL1 and along the Argens River between Verteil and PAL1 (Fig.  
644 1B). The elevation models suggest that these topographic features were largely  
645 inherited over the past 2000 years (Fig. 8B-E). More specifically, the small shallow

646 depression above sea level south of ESC1 at 500 cal yr BP (Fig. 8E) is consistent with the  
647 palaeoecological and chronological data from the ESC1 core that shows the presence of a  
648 freshwater marsh from ca. 700 to 330 cal yr BP (Allinne et al., 2006).

649

650

## 651 7. DISCUSSION

### 652 7.1. Sediment flux and fluvial activity

653 The elevation models were used to estimate late Holocene sediment fluxes in the ARDS  
654 (Fig. 9a). The total sediment flux in the confined bayhead delta was greatest from 2500  
655 to 2000 cal yr BP, with a deposition rate estimated at  $52,000 \pm 8500 \text{ m}^3.\text{yr}^{-1}$ . A decrease  
656 in total sediment flux occurred after 2000 cal yr BP, with rates ranging from  $15,800 \pm$   
657  $2300$  to  $26,700 \pm 4100 \text{ m}^3.\text{yr}^{-1}$ . The sediment flux in the unconfined bayhead delta along  
658 the modern delta front east of BN5 (Fig. 6) shows a general decrease from  $47,900 \pm$   
659  $9600$  to  $27,000 \pm 5400 \text{ m}^3.\text{yr}^{-1}$  over the last 2500 years (Fig. 9a).

660 Subaerial and subaqueous sediment fluxes in the confined bayhead delta were estimated  
661 by calculating the volume of sediments above and below sea level, respectively. The  
662 subaqueous sediment flux followed a similar trend to the total sediment flux. More  
663 specifically, the rates of subaqueous sediment flux declined sharply from  $41,200 \pm 8200$   
664 to  $18,700 \pm 3700 \text{ m}^3.\text{yr}^{-1}$  between 2500 and 1500 cal yr BP, then from  $6200 \pm 1200$  to  
665  $700 \pm 100 \text{ m}^3.\text{yr}^{-1}$  during the last millennium. Overall, the subaerial sediment flux  
666 exhibits an inverse trend with rates ranging from  $8000 \pm 1600$  to  $10,700 \pm 2100 \text{ m}^3.\text{yr}^{-1}$   
667 between 2500 and 500 cal yr BP, then increasing to  $17,800 \pm 3600 \text{ m}^3.\text{yr}^{-1}$  between 500  
668 and 0 cal yr BP (Fig. 9a). Moreover, it is worth noting that the rate of subaerial sediment  
669 flux from 2500 to 2000 cal yr BP ( $10,700 \pm 2100 \text{ m}^3.\text{yr}^{-1}$ ) was slightly higher than that  
670 from 2000 to 1500 cal yr BP ( $8000 \pm 1600 \text{ m}^3.\text{yr}^{-1}$ ).

671 The subaqueous sediment flux was ca. 2 to 4 times higher than the subaerial sediment  
672 flux between 2500 and 1500 cal yr BP, while the latter exceeded the former during the  
673 last millennium. The subaerial sediment flux was 25 times higher than the subaqueous  
674 sediment flux over the past 500 years. In fact, the rate of subaerial sediment flux  
675 increased sharply between 500 and 0 cal yr BP and was two times higher than during  
676 the period from 1000 to 500 cal yr BP. This sharp increase was associated with a slight  
677 increase in the total sediment flux of the confined bayhead delta between 500 and 0 cal  
678 yr BP, although this latter should be interpreted with caution given uncertainties of flux  
679 rates. Besides, the sediment flux of the unconfined bayhead delta does not seem to have  
680 significantly changed during the last millennium (Fig. 9a).

681 The high rates of sediment flux during the late Iron Age Cold Period (IACP) and the early  
682 Roman Warm Period (RWP) between 2500 and 2000 cal yr BP were accompanied by  
683 high levels of fluvial activity in the easternmost part of the lower Argens valley, as  
684 suggested by the geochemical indicators of riverine input from the BN1 and BN5 cores  
685 (Fig. 9b-c). The decrease in sediment fluxes between 2000 and 1500 cal yr BP was  
686 contemporaneous with a period of low fluvial activity in the second half of the RWP.  
687 Then the fluvial activity increased and was generally higher than average during the  
688 Dark Ages Cold Period (DACP), the Medieval Warm Period (MWP) and the Little Ice Age  
689 (LIA), except for BN5 over the last 300 years.

690 The periods of higher than average fluvial activity in the ARDS during the late Holocene  
691 were most often associated with high riverine flooding in the southern French Alps and,  
692 more generally, with more frequent river floods and extreme fluvial events in  
693 southeastern France (Fig. 9b-f). Overall, the Mediterranean deltas grew slowly during  
694 the Middle Ages, then high fluvial sediment supply to coast led to their rapid growth  
695 after 500 cal yr BP (Anthony et al., 2014), i.e. during the LIA and 20th century global

696 warming. In the western Mediterranean, the LIA was generally characterized by more  
697 frequent flooding and higher fluvial activity (Barriendos Vallve and Martin-Vide, 1998;  
698 Wilhelm et al., 2012; Wirth et al., 2013; Benito et al., 2015a; Degeai et al., 2017). Besides,  
699 Gutiérrez-Elorza and Pena-Monné (1998) found that climate-driven sediment  
700 accumulation in valleys from northeastern Spain was more widespread during the IACP  
701 than during the LIA, which is consistent with the pattern of total sediment flux in the  
702 ARDS (Fig. 9a).

703

## 704 7.2. Autogenic control

705 Autogenic processes play an important role in controlling the stratigraphic architecture  
706 of bayhead delta (Simms et al., 2018). For fluvio-deltaic systems developed in incised  
707 valleys, geomorphologically-driven autogenic processes such as channel avulsion,  
708 meander cutoff, increasing levee height and tributary junction can have been controlled  
709 by changes in accommodation space and valley gradient, confluence of tributary valleys,  
710 or channel extension (Vis et al., 2010; Amorosi et al., 2013a; Simms and Rodriguez,  
711 2015; Simms et al., 2018).

712 In the lower valley of the Argens River, the evolution of subaqueous sediment fluxes  
713 paralleled a progressive decrease in the mean slope of the longitudinal valley gradient  
714 and in the volume of the accommodation space, which were higher than 2.8‰ and 20  
715 Mm<sup>3</sup>, respectively, between 2500 and 2000 cal yr BP (Fig. 10a-c). The general evolution  
716 of the rates of subaqueous sediment deposition in the ARDS could therefore have been  
717 primarily driven by geomorphic factors over the last 2500 years. In general, lower rates  
718 of sediment flux into estuarine systems and late stages of sedimentary fill in a largely  
719 infilled estuarine basin, i.e. in a shallow subaqueous environment, are controlled by  
720 limited accommodation space rather than sediment flux (Clement and Fuller, 2018).

721 More specifically, the lowest rate of subaqueous sediment flux in the incised-valley  
722 system of the Argens River would have been driven by a very limited accommodation  
723 space over the last 500 years (Fig. 10b).

724 The sediment flux and fluvial activity associated with the marine environment of  
725 prodelta in unit 1 (Fig. 2, 3), which spans the period from ca. 2700 to 1800 cal yr BP  
726 from the age-elevation models (Fig. 6), were high in the late IACP then decreased during  
727 the first half of the RWP (Fig. 10c-e). This is inconsistent with the environmental  
728 evolution of western Mediterranean prodeltas, which generally show an upward  
729 increase in riverine influence (Amorosi et al., 2008, 2013c). Therefore, the period of high  
730 fluvial activity and sediment flux between 2500 and 2000 cal yr BP could be indicative of  
731 an increased fluvial sedimentation caused by allogenic forcing rather than by autogenic  
732 control during delta progradation.

733 By contrast, the increasingly strong riverine input in the easternmost part of the Argens  
734 valley from ca. 1650 to 1300 cal yr BP corresponds to the formation of a delta front,  
735 which suggests that sediment flux was mainly controlled by autogenic processes during  
736 this period (Fig. 10e). Besides, a regional increase in riverine flood frequency occurred  
737 in southeastern France during the DACP (Fig. 9d-f). Thus, the fluvial sediment supply  
738 associated with the advancing delta front could have been strengthened by an increase  
739 in riverine input in response to allogenic forcing (e.g. climate change).

740 The high fluvial activity of the DACP was maintained in the MWP from ca. 1100 to 600  
741 cal yr BP (Fig. 10e). During the period between 1500 and 500 cal yr BP, the elevation  
742 models suggest that delta progradation led to tributary junctions of the Argens, Reyran  
743 and Villepey Rivers in the easternmost part of the lower Argens valley (Fig. 8C-E). In  
744 general, the progradation rates of bayhead deltas increase when crossing  
745 geomorphologically and environmentally controlled thresholds such as tributary

746 junctions in the absence of allogenic forcing mechanisms (Simms and Rodriguez, 2015).  
747 Moreover, the fluvial sediments filling the river channels identified in BN1 and BN5  
748 cores were deposited between ca. 1350 and 450 cal yr BP and between ca. 1000 and 550  
749 cal yr BP, respectively (Fig. 2, 3, 6). Thus, the period of high fluvial activity during the  
750 MWP could have been driven by autogenic processes such as tributary junction or  
751 channel avulsion. Furthermore, each flood record in the southern Alps exhibits at least  
752 one episode of more frequent riverine flooding during the MWP (Fig. 9d-e). Therefore, it  
753 cannot be ruled out that the high levels of fluvial activity in the ARDS were partially  
754 controlled by allogenic forcing during the MWP.

755 From 500 to 0 cal yr BP, the formation of the floodplain in the easternmost part of the  
756 lower Argens valley was associated with the highest rate of subaerial sediment flux and  
757 with higher than average levels of fluvial activity (Fig. 10d-e), although the mean slope  
758 and accommodation space were very low (Fig. 10a-b). Besides, this period was  
759 characterized by high flood frequency and fluvial activity in southeastern France (Fig.  
760 9d-f). All this suggests that fluvial sedimentation in the ARDS was closely related to  
761 allogenic factors during the LIA.

762

### 763 7.3. Impact of climate change

764 The impacts of rapid climate change on vegetation cover and hydrological regime are  
765 allogenic factors that may have controlled the fluvial and coastal sedimentation in the  
766 western Mediterranean during the Holocene (Fletcher and Zielhofer, 2013). At this time,  
767 the periods of higher flood frequency in this region coincided with transitions to cool  
768 and wet climatic conditions during persistent negative phases of the North Atlantic  
769 oscillation (NAO) (Wirth et al., 2013; Benito et al., 2015a).



770 The NAO is one of the most prominent and recurrent modes of atmospheric circulation  
771 variability in Europe (Hurrell et al., 2003). A southward (northward) shift of the North  
772 Atlantic westerly winds and storm tracks during the negative (positive) phase of the  
773 NAO leads to a wetter (drier) climate in southern Europe and to a drier (wetter) climate  
774 in northern Europe (Hurrell, 1995; Serreze et al., 1997; Osborn et al., 1999; Trigo et al.,  
775 2002). A well-known speleothem record of late Holocene climate change in northwest  
776 Scotland (Fig. 1A) was supposedly driven by the bipolar seesaw of storminess and  
777 humidity related to the NAO (Proctor et al., 2002; Trouet et al., 2009). In the lower  
778 Argens valley, the episodes of high fluvial activity in the late IACP, the first half of the  
779 RWP, the DACP and the LIA occurred during dry periods in northern Europe and should  
780 thus have been associated with a southward shift of the westerly winds typically found  
781 in a negative phase of the NAO (Fig. 10e-g, 11A), except for the MWP during which the  
782 high fluvial activity was mainly driven by autogenic control due to delta progradation  
783 (see section 7.2). However, increased flood frequencies in Europe may also have been  
784 influenced by other small-scale flow patterns in the atmosphere (Jacobeit et al., 2003).  
785 Hence, we undertook an empirical orthogonal function (EOF) analysis of winter  
786 (December to February) sea level pressure (SLP) using the 500 yr data set from  
787 Luterbacher et al. (2002) in order to highlight atmospheric circulation patterns in the  
788 North Atlantic and Europe (Fig. 11). The respective contributions of the three first EOFs  
789 to the total variance are estimated at 51, 20 and 14%. The leading EOF mode (EOF1)  
790 exhibits a north-south dipole with zonal flow over Europe (Fig. 11A). This NAO-like  
791 pattern is characterized by high (low) SLP anomalies over the Icelandic Low and low  
792 (high) SLP anomalies over the Azores High during its negative (positive) phase  
793 (Luterbacher et al., 2002; Josey et al., 2011), although its southern centre is offset to the  
794 east (Fig. 1A, 11A). The second EOF mode (EOF2) shows anomalously low (high) SLP

795 over the North Sea that may be associated with the negative (positive) phase of the East  
796 Atlantic/West Russian (EA/WR) pattern (Fig. 11B) (Josey et al., 2011). The third EOF  
797 mode (EOF3) is characterized by high (low) SLP anomalies centred west of the British  
798 Isles around 55°N latitude and 25°W longitude (Fig. 11C), which correspond to the  
799 negative (positive) phase of the East Atlantic (EA) pattern (Luterbacher et al., 2002;  
800 Josey et al., 2011).

801 The EA/WR and EA patterns were mentioned as potential drivers of atmospheric  
802 circulation and climate change in western Europe during the late Holocene (Dermody et  
803 al., 2012; Moffa-Sanchez et al., 2014; Sanchez-Lopez et al., 2016; Sicre et al., 2016;  
804 Degeai et al., 2017). From observational data, the negative phases of the EA/WR and EA  
805 patterns were associated with higher precipitation and enhanced ocean heat loss in the  
806 northwestern Mediterranean (Qian et al., 2000; Josey et al., 2011), while strong (weak)  
807 surface winds in France were associated with either a negative (positive) phase of the  
808 EA/WR pattern or a positive (negative) phase of the EA pattern (Najac et al., 2009).  
809 Hence, given the late Holocene storm activity in France and the SST record in the  
810 northwestern Mediterranean (Fig. 10h-k), the late IACP should have been characterized  
811 by a negative phase of the EA pattern, then the lower RWP (upper RWP-DACP) and  
812 MWP (LIA) would have been associated with a positive (negative) phase of the EA/WR  
813 pattern (Fig. 10l).

814 In the northwestern Mediterranean, the coupling of cold northerly winds generated by  
815 winter North Atlantic blocking events due to anomalously high SLP in the eastern North  
816 Atlantic during the negative phase of the EA pattern (Shabbar et al., 2001; Jiang et al.,  
817 2003; Trigo et al., 2004; Josey et al., 2011; Moffa-Sanchez et al., 2014; Sanchez-Lopez et  
818 al., 2016; Sicre et al., 2016) with warm and dry summer due to the northward position of  
819 the ITCZ (Goudeau et al., 2015) could have led to enhanced convection and higher

820 rainfall along the southern Alps in the late IACP (Fig. 10l-m, 11C), similarly to modern  
821 heavy precipitating systems over southeastern France (Nuissier et al., 2008; Duffourg  
822 and Ducrocq, 2011). This synoptic situation could explain the high fluvial activity and  
823 sediment flux in the ARDS during the late IACP (Fig. 10e).

824 The positive phase of the EA/WR pattern in the lower RWP from ca. 2300 to 1800 cal yr  
825 BP was associated with a large-scale circulation pattern characterized by a negative or  
826 positive phase of the NAO (Fig. 10g, l). This period shows a decreasing trend in fluvial  
827 activity in the ARDS apart from the 2nd and 1st centuries BCE (Fig. 10e). The ITCZ was  
828 still in a northern position during the lower RWP, but the absence or low frequency of  
829 atmospheric blocking events and cold northerly winds would have limited atmospheric  
830 convection and precipitation in the southern Alps at this time. During the late RWP and  
831 the DACP from 1800 to 1150 cal yr BP, the negative phase of the EA/WR pattern  
832 corresponded to a general increase in fluvial activity in the ARDS, with higher than  
833 average values when the negative phases of the EA/WR and NAO patterns were coupled  
834 in the late DACP between 1600 and 1150 cal yr BP (Fig. 10e, g, l, 11B).

835 In the Western Mediterranean, there is a broad consensus on the climatic conditions of  
836 the MWP (LIA), which were generally warm (cold) and dry (wet) from continental  
837 records in Spain (Martin-Puertas et al., 2008, 2010; Martin-Chivelet et al., 2011; Moreno  
838 et al., 2012; Sanchez-Lopez et al., 2016), Italy (Frisia et al., 2005; Mensing et al., 2016;  
839 Sadori et al., 2016), southern France (Degeai et al., 2017) and northern Morocco  
840 (Wassenburg et al., 2013). Overall, the MWP (LIA) would have been characterized by the  
841 combination of a positive (negative) phase of the NAO with a positive (negative) phase  
842 of the EA/WR pattern (Fig. 10g, l).

843 The climatic context of the LIA would have been similar to that of the DACP (Fig. 11B).

844 During the cold and humid period of the LIA, high detrital inputs of terrigenous material

845 were identified in marine sediments from the western Mediterranean basin (Fig. 1A).  
846 Interestingly, the sharp increase in subaerial sediment flux in the ARDS after 500 cal yr  
847 BP is consistent with this high offshore discharge of riverine sediment (Fig. 10d).  
848 Overall, the LIA was characterized by high fluvial sediment supply to Mediterranean  
849 deltas in an increasingly human-influenced environment (Anthony et al., 2014).  
850 However, it is currently difficult to assess the real contribution of human land use to late  
851 Holocene sediment flux in the ARDS because of the lack of quantitative data to measure  
852 the magnitude of the geomorphic impact of anthropogenic forcing.  
853 Finally, the climate-driven fluvial activity in the ARDS over the past 2500 years would  
854 have been higher than average when the negative phase of the NAO-like pattern was  
855 associated with either a negative phase of the EA/WR pattern or the combination of a  
856 negative EA pattern with a northward migration of the ITCZ.

857

858

## 859 8. CONCLUSION

860 The elevation modelling and palaeogeographic reconstruction of incised valleys in  
861 coastal areas is challenging because this kind of environment is often characterized by  
862 rapid changes in relative sea level, shoreline progradation, delta sedimentation and  
863 climatic conditions. A new multi-method approach using cores and archaeological  
864 trenches, geochemistry and magnetic susceptibility of sediments, malacology,  
865 radiocarbon chronology, geostatistics and numerical modelling was undertaken in order  
866 to robustly characterize changes in environmental conditions, geomorphic setting and  
867 sediment flux associated with delta growth in incised-valley systems. This quantitative  
868 method was applied to the bayhead delta of the Argens River in the western

869 Mediterranean, in order to assess the impacts of autogenic control and climate change  
870 on the variations in sediment flux and fluvial activity of this deltaic system.

871 The coastal dynamics of the Argens River delta system were studied over the last 2500  
872 years. The sedimentary successions of this deltaic depositional system revealed four  
873 major facies associations from bottom to top: (1) a prodelta with clay-sand alternations  
874 deposited in a marine environment with brackish or freshwater influences and high  
875 levels of salinity, (2) a delta front characterized by higher sand content as well as by  
876 coarsening-upward trend and gradual increase in riverine input, (3) river channels filled  
877 with sand and gravel, and (4) a floodplain with a high abundance of land snails and low  
878 salinity levels.

879 Late Holocene sediment fluxes were estimated from numerical modelling then  
880 compared with hydroclimate proxy records and geomorphic factors. An overall decrease  
881 in subaqueous sediment supply over the last 2500 years could have been  
882 geomorphologically controlled by autogenic processes such as changes in  
883 accommodation space and delta slope. High rates of sediment flux between 2500 and  
884 2000 cal yr BP coincided with higher precipitation and more frequent riverine flooding  
885 in the western Mediterranean. The maximum rate of subaerial sediment flux from 500 to  
886 0 cal yr BP could have been caused by higher fluvial activity and more frequent flood  
887 events during the cold and wet climatic conditions of the Little Ice Age.

888 In general, the high sediment fluxes at 2500-2000 and 500-0 cal yr BP were associated  
889 with higher than average levels of fluvial activity in the Argens River delta system. The  
890 periods of high fluvial activity driven by climate change were associated with a  
891 southward shift of the North Atlantic westerlies and storm tracks in southern Europe.

892 This atmospheric circulation pattern was combined with either (1) a negative phase of  
893 the East Atlantic pattern coupled to a northward migration of the intertropical

894 convergence zone in the late Iron Age Cold Period, or (2) a negative phase of the East  
895 Atlantic/West Russian pattern during the Dark Ages Cold Period and Little Ice Age.  
896 This quantitative approach will need to be applied to other Mediterranean deltas in  
897 order to compare the variation of coastal sediment fluxes in response to hydroclimate  
898 change and geomorphic setting over the past millennia. Besides, the study of other  
899 deltaic sequences will be needed to firmly establish a link between delta sedimentation  
900 and atmospheric circulation patterns in the western Mediterranean. Furthermore, the  
901 analysis of palaeobotanical, archaeological and historical data will be required to  
902 accurately estimate the impact of human land use on sediment flux and geomorphic  
903 change in these coastal areas.

904

#### 905 Acknowledgments

906 This work is a part of a research program financially supported by the CNRS and the  
907 French Ministry of Culture and Communication. The BN1 and BN5 cores were  
908 undertaken by the CETE Méditerranée, the C2FN (DT INSU, CNRS, EQUIPEX CLIMCOR,  
909 Investissements d'Avenir ANR-11-EQPX-0009) and the BRGM. The sedimentological  
910 analyses were done at the ArcheoEnvironnement Laboratory (CNRS UMR5140). We  
911 thank Dr. Edward Anthony (editor) and two anonymous reviewers for their helpful  
912 remarks and suggestions that improved the manuscript.

913

914

#### 915 Data availability

916 <http://dx.doi.org/10.17632/p5fbtmwnsr.1>

917

918

919 References

920

921 Allinne, C., Devillers, B., Bertoncello, F., Bouby, L., Bruneton, H., Bui Thi, M., Cade, C.,  
922 Revil, A., 2006. Archéologie et paléoenvironnement sur le site du pont romain des  
923 Esclapes (Fréjus, Var). *ArcheoSciences* 30, 181-196.

924 Amorosi, A., Milli, S., 2001. Late Quaternary depositional architecture of Po and Tevere  
925 river deltas (Italy) and worldwide comparison with coeval deltaic successions.  
926 *Sediment. Geol.* 144, 357-375.

927 Amorosi, A., Centineo, M.C., Colalongo, M.L., Fiorini, F., 2005. Millennial-scale  
928 depositional cycles from the Holocene of the Po Plain, Italy. *Mar. Geol.* 222-223, 7-18.

929 Amorosi, A., Dinelli, E., Rossi, V., Vaiani, S.C., Sacchetto, M., 2008. Late Quaternary  
930 palaeoenvironmental evolution of the Adriatic coastal plain and the onset of Po River  
931 Delta. *Palaeogeogr. Palaeoclim. Palaeoecol.* 268, 80-90.

932 Amorosi, A., Lucchi, M.R., Rossi, V., Sarti, G., 2009. Climate change signature of small-  
933 scale parasequences from Lateglacial–Holocene transgressive deposits of the Arno  
934 valley fill. *Palaeogeogr. Palaeoclim. Palaeoecol.* 273, 142-152.

935 Amorosi, A., Bini, M., Giacomelli, S., Pappalardo, M., Ribecai, C., Rossi, V., Sammartino, I.,  
936 Sarti, G., 2013a. Middle to late Holocene environmental evolution of the Pisa coastal  
937 plain (Tuscany, Italy) and early human settlements. *Quat. Int.* 303, 93-106.

938 Amorosi, A., Rossi, V., Sarti, G., Mattei, R., 2013b. Coalescent valley fills from the late  
939 Quaternary record of Tuscany (Italy). *Quat. Int.* 288, 129-138.

940 Amorosi, A., Rossi, V., Vella, C., 2013c. Stepwise post-glacial transgression in the Rhône  
941 Delta area as revealed by high-resolution core data. *Palaeogeogr. Palaeoclim.*  
942 *Palaeoecol.* 374, 314-326.

943 Amorosi, A., Bracone, V., Campo, B., D'Amico, C., Rossi, V., Roskopf, C.M., 2016. A late  
944 Quaternary multiple paleovalley system from the Adriatic coastal plain (Biferno  
945 River, Southern Italy). *Geomorphology* 254, 146-159.

946 Anthony, E.J., 2015. Wave influence in the construction, shaping and destruction of river  
947 deltas: a review. *Mar. Geol.* 361, 53-78.

948 Anthony, E.J., Marriner, N., Morhange, C., 2014. Human influence and the changing  
949 geomorphology of Mediterranean deltas and coasts over the last 6000 years: From  
950 progradation to destruction phase? *Earth Sci. Rev.* 139, 336-361.

951 Arnaud-Fassetta, G., Carcaud, N., Castanet, C., Salvador, P.-G., 2010. Fluvial  
952 palaeoenvironments in archaeological context: Geographical position, methodological  
953 approach – Hydrological risk issues. *Quat. Int.* 216, 93-117.

954 Barriendos Vallve, M., Martin-Vide, J., 1998. Secular climatic oscillations as indicated by  
955 catastrophic floods in the Spanish Mediterranean coastal area (14th–19th centuries).  
956 *Climatic Change* 38, 473-491.

957 Benito, G., Macklin, M.G., Zielhofer, C., Jones, A.F., Machado, M.J., 2015a. Holocene  
958 flooding and climate change in the Mediterranean. *Catena* 130, 13-33.

959 Benito, G., Macklin, M.G., Panin, A., Rossato, S., Fontana, A., Jones, A.F., Machado, M.J.,  
960 Matlakhova, E., Mozzi, P., Zielhofer, C., 2015b. Recurring flood distribution patterns  
961 related to short-term Holocene climatic variability. *Sci. Rep.* 5(16398), 1-8.

962 Bertoncello, F., Bonnet, S., Bouby, L., Delhon, C., Devillers, B., Guillon, S., 2008. *Projet*  
963 *Collectif de Recherches « Occupation du sol et patrimoine archéologique dans la basse*  
964 *vallée de l'Argens »*. *Rapport de fin de projet*. Rapport pour le Ministère de la Culture et  
965 de la Communication, CEPAM, Nice, 124 p.

966 Bertoncello, F., Bonnet, S., Excoffon, P., Bony, G., Morhange, C., Gébara, C., Georges, K.,  
967 Devillers, B., 2011. Dynamique du littoral et peuplement : le cas de la colonie romaine



968 de Fréjus. In Pasqualini, M. (Ed.): *Fréjus romaine, la ville et son territoire.*  
969 *Agglomérations de Narbonnaise, des Alpes-Maritimes et de Cisalpine à travers la*  
970 *recherche archéologique.* Editions APDCA, Antibes, 75-87.

971 Bertoncello, F., Fovet, E., Tannier, C., Gandini, C., Lautier, L., Nouvel, P., Nuninger, L.,  
972 2012. Configurations spatiales et hiérarchiques du peuplement antique : des  
973 indicateurs quantitatifs pour une confrontation interrégionale. In Bertoncello, F.,  
974 Braemer, F. (Eds.): *Variabilités Environnementales, Mutations sociales : Nature,*  
975 *Intensités, Échelles et Temporalités des changements.* Editions APDCA, Antibes, 175-  
976 190.

977 Bertoncello, F., Devillers, B., Bonnet, S., Guillon, S., Bouby, L., Delhon, C., 2014a. Mobilité  
978 des paysages littoraux et peuplement dans la basse vallée de l'Argens (Var, France) au  
979 cours de l'Holocène. *Quaternaire* 25 (1), 23-44.

980 Bertoncello, F., Burri, S., Delhon, C., Digelmann, P., Bernigaud, N., Borréani, M., Gébara, C.,  
981 Portalier, N., Purdue, L., 2014b. *Projet Collectif de Recherches « Dynamiques du*  
982 *peuplement et des paysages dans le territoire de Fréjus ».* Rapport d'activité 2014 et  
983 *projet 2015-2016.* Rapport pour le Ministère de la Culture et de la Communication,  
984 CEPAM, Nice, 38 p.

985 Bertoncello, F., Bernigaud, N., Burri, S., Degeai, J.-P., Delhon, C., Digelmann, P., Gayet, F.,  
986 Jansen, P., Mercuri, L., Ouriachi, M.-J., Porra, M., Portalier, N., Purdue, L., Romagnan, B.,  
987 Segura, J.-A., Vaschalde, C., 2016. *Projet Collectif de Recherches, Dynamiques du*  
988 *peuplement et des paysages dans le territoire de Fréjus. Rapport final 2014-2016.*  
989 Rapport pour le Ministère de la Culture et de la Communication, CEPAM, Nice, 115 p.

990 Bony, G., Morhange, C., Bruneton, H., Carbonel, P., Gébara, C., 2011. 2000 ans de  
991 colmatage du port antique de Fréjus (*Forum Julii*), France : une double métamorphose  
992 littorale. *CR Geosci.* 343, 701-715.

- 993 Chagué-Goff, C., Dawson, S., Goff, J.R., Zachariassen, J., Berryman, K.R., Garnett, D.L.,  
994 Waldron, H.M., Mildenhall, D.C., 2002. A tsunami (ca. 6300 years BP) and other  
995 Holocene environmental changes, northern Hawke's Bay, New Zealand. *Sediment.*  
996 *Geol.* 150, 89-102.
- 997 Clement, A.J.H., Fuller, I.C., 2018. Influence of system controls on the Late Quaternary  
998 geomorphic evolution of a rapidly-infilled incised-valley system: The lower  
999 Manawatu valley, North Island New Zealand. *Geomorphology* 303, 13-29.
- 1000 Cohen, O., 1997. La baie de Fréjus : 2000 ans d'évolution du rivage. *Mappemonde* 1, 6-12.
- 1001 Croudace, I.W., Rindby, A., Rothwell, R.G., 2006. ITRAX: description and evaluation of a  
1002 new multi-function X-ray core scanner. In Rothwell, R.G. (ed.): *New techniques in*  
1003 *sediment core analysis*. Geological Society, London, Special Publications 267, 51-63.
- 1004 Dalrymple, R.W., Zaitlin, B.A., Boyd, R., 1992. Estuarine facies models: conceptual basis  
1005 and stratigraphic implications. *J. Sediment. Petrol.* 62 (6), 1130-1146.
- 1006 Dearing, J., 1999. *Environmental magnetic susceptibility using the Bartington MS2 system*.  
1007 Bartington Instruments, Oxford, 43 p.
- 1008 Degeai, J.-P., Devillers, B., Dezileau, L., Oueslati, H., Bony, G., 2015. Major storm periods  
1009 and climate forcing in the Western Mediterranean during the Late Holocene. *Quat. Sci.*  
1010 *Rev.* 129, 37-56.
- 1011 Degeai, J.-P., Devillers, B., Blanchemanche, P., Dezileau, L., Oueslati, H., Tillier, M., Bohbot,  
1012 H., 2017. Fluvial response to the last Holocene rapid climate change in the  
1013 Northwestern Mediterranean coastlands. *Glob. Planet. Chang.* 152, 176-186.
- 1014 Delile, H., Abichou, A., Gadhoun, A., Goiran, J.-P., Pleuger, E., Monchambert, J.-Y., Wilson,  
1015 A., Fentress, E., Quinn, J., Ben Jerbania, I., Ghozzi, F., 2015. The geoarchaeology of  
1016 Utica, Tunisia: the paleogeography of the Mejerda Delta and hypotheses concerning  
1017 the location of the ancient harbour. *Geoarchaeology* 30, 291-306.

1018 Dermody, B.J., De Boer, H.J., Bierkens, M.F.P., Weber, S.L., Wassen, M.J., Dekker, S.C., 2012.  
1019 A seesaw in Mediterranean precipitation during the Roman Period linked to  
1020 millennial-scale changes in the North Atlantic. *Clim. Past* 8, 637-651.

1021 Devillers, B., Bonnet, S., 2006. 6000 ans d'histoire environnementale de la lagune de  
1022 Villepey (Fréjus, Var) : premiers résultats de l'étude multi-proxies de la carotte Vil2.  
1023 *ArcheoSciences* 30, 197-203.

1024 Devillers, B., Excoffon, P., Morhange, C., Bonnet, S., Bertoncello, F., 2007. Relative sea-  
1025 level changes and coastal evolution at *Forum Julii* (Fréjus, Provence). *CR Geosci.* 339,  
1026 329-336.

1027 Devillers, B., Bony, G., Degeai, J.-P., Gasco, J., Lachenal, T., Bruneton, H., Yung, F., Oueslati,  
1028 H., Thierry, A., 2019. Holocene coastal environmental changes and human occupation  
1029 of the lower Hérault River, southern France. *Quat. Sci. Rev.* 222, 105912.

1030 Dezileau, L., Sabatier, P., Blanchemanche, P., Joly, B., Swingedouw, D., Cassou, C.,  
1031 Castaings, J., Martinez, P., Von Grafenstein, U., 2011. Intense storm activity during the  
1032 Little Ice Age on the French Mediterranean coast. *Palaeogeogr. Palaeoclim. Palaeoecol.*  
1033 299, 289-297.

1034 Dezileau, L., Pérez-Ruzafa, A., Blanchemanche, P., Degeai, J.-P., Raji, O., Martinez, P.,  
1035 Marcos, C., Von Grafenstein, U., 2016. Extreme storms during the last 6500 years from  
1036 lagoonal sedimentary archives in the Mar Menor (SE Spain). *Clim. Past* 12, 1389-1400.

1037 Dubar, M., 2004. L'édification de la plaine deltaïque du Bas Argens (Var, France) durant  
1038 la Protohistoire et l'Antiquité. Application d'un modèle numérique 2D à l'archéologie.  
1039 *Méditerranée* 102, 47-54.

1040 Dubar M., Anthony, E.J., 1995. Holocene environmental change and river-mouth  
1041 sedimentation in the Baie des Anges, French Riviera. *Quat. Res.* 43, 329-343.

- 1042 Dubar, M., Bui-Thi, M., Nicol-Pichard, S., Thinon, M., 2004. Étude palynologique du  
1043 carottage de Pont d'Argens (Roquebrune-sur-Argens, Var) : histoire holocène de la  
1044 végétation en Provence cristalline ; facteurs naturels et anthropiques. *Ecologia*  
1045 *Mediterranea* 30 (2), 147-157.
- 1046 Duffourg, F., Ducrocq, V., 2011. Origin of the moisture feeding the Heavy Precipitating  
1047 Systems over Southeastern France. *Nat. Hazards Earth Syst. Sci.* 11, 1163-1178.
- 1048 Durozoy, G., Gouvernet, C., Jonquet, P., Theillier, P., 1970. *Inventaire des ressources*  
1049 *hydrauliques dans la basse vallée de l'Argens (Var)*. BRGM, Orléans, 39 p.
- 1050 EPA, 2007. *Method 6200: Field portable X-ray fluorescence spectrometry for the*  
1051 *determination of elemental concentrations in soil and sediment*. United States  
1052 Environmental Protection Agency, 32 p.,  
1053 <https://www.epa.gov/sites/production/files/2015-12/documents/6200.pdf>
- 1054 Excoffon, P., Devillers, B., Bonnet, S., Bouby, L., 2006. Nouvelles données sur la position  
1055 du littoral antique de Fréjus. Le diagnostic archéologique du "théâtre  
1056 d'agglomération" (Fréjus, Var). *ArcheoSciences* 30, 205-221.
- 1057 Excoffon, P., Bonnet, S., Devillers, B., Berger, J.-F., 2010. L'évolution de trait de côte aux  
1058 abords de Fréjus, de sa foundation jusqu'à la fin du I<sup>er</sup> siècle après J.-C. In: Delestre, X.,  
1059 Marchesi, H. (Eds.), *Archéologie des rivages méditerranéens : 50 ans de recherche. Actes*  
1060 *du colloque d'Arles (Bouches-du-Rhône) 28-29-30 octobre 2009*. Errance, Paris, 47-53.
- 1061 Fletcher, W.J., Zielhofer, C., 2013. Fragility of Western Mediterranean landscapes during  
1062 Holocene Rapid Climate Changes. *Catena* 103, 16-29.
- 1063 Fletcher, W.J., Debret, M., Sanchez-Goni, M.F., 2013. Mid-Holocene emergence of a low-  
1064 frequency millennial oscillation in western Mediterranean climate: Implications for  
1065 past dynamics of the North Atlantic atmospheric westerlies. *The Holocene* 23(2), 153-  
1066 166.

1067 Fontugne, M., 2004. Les derniers progrès du calibrage des âges radiocarbone  
1068 permettent-ils une révision des chronologies entre 25 et 50.000 ans B.P. ?  
1069 *Quaternaire* 15 (3), 245-252.

1070 Frigola, J., Moreno, A., Cacho, I., Canals, M., Sierro, F.J., Flores, J.A., Grimalt, J.O., Hodell,  
1071 D.A., Curtis, J.H., 2007. Holocene climate variability in the western Mediterranean  
1072 region from a deepwater sediment record. *Paleoceanography* 22, PA2209.

1073 Frisia, S., Borsato, A., Spötl, C., Villa, I.M., Cucchi, F., 2005. Climate variability in the SE  
1074 Alps of Italy over the past 17 000 years reconstructed from a stalagmite record.  
1075 *Boreas* 34, 445-455.

1076 Gascou, J., 1982. Quand la colonie de Fréjus fut-elle fondée ? *Latomus* 41(1), 132-145.

1077 Gascou, J., Janon, M., 1985. Inscriptions Latines de Narbonnaise (I.L.N.)- Fréjus. *Gallia*  
1078 Suppl. 44, 229 p.

1079 Gébara, C., Morhange, C., 2010. Fréjus (*Forum Julii*): le port antique/the ancient harbour.  
1080 *J. Roman Archaeol.* Suppl. 77, 152 p.

1081 Giaime, M., Marriner, N., Morhange, C., 2019. Evolution of ancient harbours in deltaic  
1082 contexts: a geoarchaeological typology. *Earth Sci. Rev.* 191, 141-167.

1083 Giraudi, C., Tata, C., Paroli, L., 2009. Late Holocene Evolution of Tiber River Delta and  
1084 Geoarchaeology of Claudius and Trajan Harbor, Rome. *Geoarchaeology* 24 (3), 371-  
1085 382.

1086 Goudeau, M.-L.S., Grauel, A.-L., Tessarolo, C., Leider, A., Chen, L., Bernasconi, S.M.,  
1087 Versteegh, G.J.M., Zonneveld, K.A.F., Boer, W., Alonso-Hernandez, C.M., De Lange, G.J.,  
1088 2014. The Glacial-Interglacial transition and Holocene environmental changes in  
1089 sediments from the Gulf of Taranto, central Mediterranean. *Mar. Geol.* 348, 88-102.

1090 Goudeau, M.-L.S., Reichart, G.-J., Wit, J.C., De Nooijer, L.J., Grauel, A.-L., Bernasconi, S.M.,  
1091 De Lange, G.J., 2015. Seasonality variations in the Central Mediterranean during

1092 climate change events in the Late Holocene. *Palaeogeogr. Palaeoclim. Palaeoecol.* 418,  
1093 304-318.

1094 Grimm, E.C., 1987. Coniss: a Fortran 77 program for stratigraphically constrained cluster  
1095 analysis by the method of incremental sum of squares. *Comput. Geosci.* 13 (1), 13-35.

1096 Grove, A.T., 2001. The "Little Ice Age" and its geomorphological consequences in  
1097 Mediterranean Europe. *Climatic Change* 48, 121-136.

1098 Gutiérrez-Elorza, M., Pena-Monné, J.L., 1998. Geomorphology and late Holocene climatic  
1099 change in Northeastern Spain. *Geomorphology* 23, 205-217.

1100 Haenssler, E., Nadeau, M.-J., Vött, A., Unkel, I., 2013. Natural and human induced  
1101 environmental changes preserved in a Holocene sediment sequence from the Etoliko  
1102 Lagoon, Greece: New evidence from geochemical proxies. *Quat. Int.* 308-309, 89-104.

1103 Hurrell, J.W., 1995. Decadal trends in the North Atlantic Oscillation: regional  
1104 temperatures and precipitation. *Science* 269, 676-679.

1105 Hurrell, J.W., Kushnir, Y., Ottersen, G., Visbeck, M., 2003. An overview of the North  
1106 Atlantic Oscillation. In: Hurrell, J.W., Kushnir, Y., Ottersen, G., Visbeck, M. (Eds.), *The*  
1107 *North Atlantic Oscillation: Climatic significance and environmental impact*. American  
1108 Geophysical Union, Washington D.C., Geophysical Monograph 134, 1-35.

1109 Jacobeit, J., Glaser, R., Luterbacher, J., Wanner, H., 2003. Links between flood events in  
1110 central Europe since AD 1500 and large-scale atmospheric circulation modes.  
1111 *Geophys. Res. Lett.* 30 (4), 1172.

1112 Jalali, B., Sicre, M.-A., Bassetti, M.-A., Kallel, N., 2016. Holocene climate variability in the  
1113 North-Western Mediterranean Sea (Gulf of Lions). *Clim. Past* 12, 91-101.

1114 Jiang, Q., Smith, R.B., Doyle, J., 2003. The nature of the mistral: Observations and  
1115 modelling of two MAP events. *Q. J. Roy. Meteorol. Soc.* 129, 857-875.

1116 Josey, S.A., Somot, S., Tsimplis, M., 2011. Impacts of atmospheric modes of variability on  
1117 Mediterranean Sea surface heat exchange. *J. Geophys. Res.-Oceans* 116, C02032.

1118 Koster, K., Stafleu, J., Cohen, K.M., 2017. Generic 3D interpolation of Holocene base-level  
1119 rise and provision of accommodation space, developed for the Netherlands coastal  
1120 plain and infilled palaeovalleys. *Basin Res.* 29, 775-797.

1121 Lambeck, K., Bard, E., 2000. Sea-level change along the French Mediterranean coast for  
1122 the past 30 000 years. *Earth Planet. Sci. Lett.* 175, 203-222.

1123 Lopez-Buendia, A.M., Bastida, J., Querol, X., Whateley, M.K.G., 1999. Geochemical data as  
1124 indicators of palaeosalinity in coastal organic-rich sediments. *Chem. Geol.* 157, 235-  
1125 254.

1126 Luterbacher, J., Xoplaki, E., Dietrich, D., Rickli, R., Jacobeit, J., Beck, C., Gyalistras, D.,  
1127 Schmutz, C., Wanner, H., 2002. Reconstruction of sea level pressure fields over the  
1128 Eastern North Atlantic and Europe back to 1500. *Clim. Dynam.* 18, 545-561.

1129 Makclin, M.G., Benito, G., Gregory, K.J., Johnstone, E., Lewin, J., Michczynska, D.J., Soja, R.,  
1130 Starkel, L., Thorndycraft, V.R., 2006. Past hydrological events reflected in the  
1131 Holocene fluvial record of Europe. *Catena* 66, 145-154.

1132 Martin-Chivelet, J., Munoz-Garcia, M.B., Edwards, R.L., Turrero, M.J., Ortega, A.I., 2011.  
1133 Land surface temperature changes in Northern Iberia since 4000 yr BP, based on  
1134  $\delta^{13}\text{C}$  of speleothems. *Glob. Planet. Change* 77, 1-12.

1135 Martinez-Ruiz, F., Kastner, M., Gallego-Torres, D., Rodrigo-Gamiz, M., Nieto-Moreno, V.,  
1136 Ortega-Huertas, M., 2015. Paleoclimate and paleoceanography over the past 20,000  
1137 yr in the Mediterranean Sea Basins as indicated by sediment elemental proxies. *Quat.*  
1138 *Sci. Rev.* 107, 25-46.

1139 Martin-Puertas, C., Valero-Garcés, B.L., Mata, M.P., Gonzalez-Sampériz, P., Bao, R.,  
1140 Moreno, A., Stefanova, V., 2008. Arid and humid phases in southern Spain during the  
1141 last 4000 years: the Zonar Lake record, Cordoba. *Holocene* 18 (6), 907-921.

1142 Martin-Puertas, C., Jiménez-Espejo, F., Martínez-Ruiz, F., Nieto-Moreno, V., Rodrigo, M.,  
1143 Mata, M.P., Valero-Garcés, B.L., 2010. Late Holocene climate variability in the  
1144 southwestern Mediterranean region: an integrated marine and terrestrial  
1145 geochemical approach. *Clim. Past* 6, 807-816.

1146 Martin-Puertas, C., Valero-Garcés, B.L., Mata, M.P., Moreno, A., Giralt, S., Martínez-Ruiz, F.,  
1147 Jiménez-Espejo, F., 2011. Geochemical processes in a Mediterranean Lake: a high-  
1148 resolution study of the last 4,000 years in Zonar Lake, southern Spain. *J. Paleolimnol.*  
1149 46, 405-421.

1150 Melis, R.T., Di Rita, F., French, C., Marriner, N., Montis, F., Serreli, G., Sulas, F., Vacchi, M.,  
1151 2018. 8000 years of coastal changes on a western Mediterranean island: A multiproxy  
1152 approach from the Posada plain of Sardinia. *Mar. Geol.* 403, 93-108.

1153 Mensing, S., Tunno, I., Cifani, G., Passigli, S., Noble, P., Archer, C., Piovesan, G., 2016.  
1154 Human and climatically induced environmental change in the Mediterranean during  
1155 the Medieval Climate Anomaly and Little Ice Age: A case from central Italy.  
1156 *Anthropocene* 15, 49-59.

1157 Milli, S., D'Ambrogi, C., Bellotti, P., Calderoni, G., Carboni, M.G., Celant, A., Di Bella, L., Di  
1158 Rita, F., Frezza, V., Magri, D., Pichezzi, R.M., Ricci, V., 2013. The transition from wave-  
1159 dominated estuary to wave-dominated delta: The Late Quaternary stratigraphic  
1160 architecture of Tiber River deltaic succession (Italy). *Sediment. Geol.* 284-285, 159-  
1161 180.



1162 Moffa-Sanchez, P., Born, A., Hall, I.R., Thornalley, D.J.R., Barker, S., 2014. Solar forcing of  
1163 North Atlantic surface temperature and salinity over the past millennium. *Nat. Geosci.*  
1164 7, 275-278.

1165 Moreno, A., Pérez, A., Frigola, J., Nieto-Moreno, V., Rodrigo-Gámiz, M., Martrat, B.,  
1166 González-Sampériz, P., Morellón, M., Martín-Puertas, C., Corella, J.P., Belmonte, A.,  
1167 Sancho, C., Cacho, I., Herrera, G., Canals, M., Grimalt, J.O., Jiménez-Espejo, F., Martínez-  
1168 Ruiz, F., Vegas-Vilarrúbia, T., Valero-Garcés, B.L., 2012. The Medieval Climate  
1169 Anomaly in the Iberian Peninsula reconstructed from marine and lake records. *Quat.*  
1170 *Sci. Rev.* 43, 16-32.

1171 Morhange, C., Marriner, N., Excoffon, P., Bonnet, S., Flaux, C., Zibrowius, H., Goiran, J.-P., El  
1172 Amouri, M., 2013. Relative sea-level changes during Roman times in the Northwest  
1173 Mediterranean: the 1st century A.D. fish tank of *Forum Julii*, Fréjus, France.  
1174 *Geoarchaeology* 28 (4), 363-372.

1175 Morhange, C., Marriner, N., 2015. Archeological and biological relative sea-level  
1176 indicators. In Shennan, I., Long, A.J., Horton, B.P. (Eds): *Handbook of sea-level research*.  
1177 AGU, Wiley, Wiley Works Series, 146-156.

1178 Najac, J., Boé, J., Terray, L., 2009. A multi-model ensemble approach for assessment of  
1179 climate change impact on surface winds in France. *Clim. Dynam.* 32, 615-634.

1180 Nieto-Moreno, V., Martinez-Ruiz, F., Giral, S., Jiménez-Espejo, F., Gallego-Torres, D.,  
1181 Rodrigo-Gamiz, M., Garcia-Orellana, J., Ortega-Huertas, M., de Lange, G.J., 2011.  
1182 Tracking climate variability in the western Mediterranean during the Late Holocene:  
1183 a multiproxy approach. *Clim. Past* 7, 1395-1414.

1184 Nieto-Moreno, V., Martinez-Ruiz, F., Giral, S., Gallego-Torres, D., Garcia-Orellana, J.,  
1185 Masqué, P., Ortega-Huertas, M., 2013a. Climate imprints during the 'Medieval Climate

1186 Anomaly' and the 'Little Ice Age' in marine records from the Alboran Sea basin. *The*  
1187 *Holocene* 23 (9), 1227-1237.

1188 Nieto-Moreno, V., Martinez-Ruiz, F., Willmott, V., Garcia-Orellana, J., Masqué, P.,  
1189 Sinninghe Damsté, J.S., 2013b. Climate conditions in the westernmost Mediterranean  
1190 over the last two millennia: An integrated biomarker approach. *Org. Geochem.* 55, 1-  
1191 10.

1192 Nuissier, O., Ducrocq, V., Ricard, D., Lebeaupin, C., Anquetin, S., 2008. A numerical study  
1193 of three catastrophic precipitating events over southern France. I: Numerical  
1194 framework and synoptic ingredients. *Q. J. Roy. Meteorol. Soc.* 134, 111-130.

1195 Osborn, T.J., Briffa, K.R., Tett, S.F.B., Jones, P.D., Trigo, R.M., 1999. Evaluation of the North  
1196 Atlantic Oscillation as simulated by a coupled climate model. *Clim. Dynam.* 15, 586-  
1197 702.

1198 Paillard, D., Labeyrie, L., Yiou, P., 1996. Macintosh program performs time-series  
1199 analysis. *EOS Transactions AGU* 77 (39), 379-379.

1200 Peltier, W.R., 2004. Global glacial isostasy and the surface of the ice-age Earth: The ICE-  
1201 5G (VM2) model and GRACE. *Annu. Rev. Earth Planet. Sci.* 32, 111-149.

1202 Proctor, C.J., Baker, A., Barnes, W.L., 2002. A three thousand year record of North  
1203 Atlantic climate. *Clim. Dynam.* 19, 449-454.

1204 Qian, B., Corte-Real, J., Xu, H., 2000. Is the North Atlantic Oscillation the most important  
1205 atmospheric pattern for precipitation in Europe? *J. Geophys. Res.* 105, 11,901-11,910.

1206 Reimer, P.J., Bard, E., Bayliss, A., Beck, J.W., Blackwell, P.G., Ramsey, C.B., Buck, C.E.,  
1207 Cheng, H., Edwards, R.L., Friedrich, M., Grootes, P.M., Guilderson, T.P., Haflidason, H.,  
1208 Hajdas, I., Hatté, C., Heaton, T.J., Hoffmann, D.L., Hogg, A.G., Hughen, K.A., Kaiser, K.F.,  
1209 Kromer, B., Manning, S.W., Niu, M., Reimer, R.W., Richards, D.A., Scott, E.M., Southon,  
1210 J.R., Staff, R.A., Turney, C.S.M., Van der Plicht, J., 2013. Intcal13 and Marine13

1211 radiocarbon age calibration curves 0-50,000 years cal BP. *Radiocarbon* 55 (4), 1869-  
1212 1887.

1213 Rodrigo-Gamiz, M., Martinez-Ruiz, F., Jiménez-Espejo, F.J., Gallego-Torres, D., Nieto-  
1214 Moreno, V., Romero, O., Ariztegui, D., 2011. Impact of climate variability in the  
1215 western Mediterranean during the last 20,000 years: oceanic and atmospheric  
1216 responses. *Quat. Sci. Rev.* 30, 2018–2034.

1217 Rodrigo-Gamiz, M., Martinez-Ruiz, F., Rodriguez-Tovar, F.J., Jimenez-Espejo, F.J., Pardo-  
1218 Iguzquiza, E., 2014. Millennial- to centennial-scale climate periodicities and forcing  
1219 mechanisms in the westernmost Mediterranean for the past 20,000 yr. *Quat. Res.* 81,  
1220 78–93.

1221 Ruiz-Pérez, J.-M., Carmona, P., 2019. Turia river delta and coastal barrier-lagoon of  
1222 Valencia (Mediterranean coast of Spain): Geomorphological processes and global  
1223 climate fluctuations since Iberian-Roman times. *Quat. Sci. Rev.* 219, 84-101.

1224 Sabatier, P., Dezileau, L., Condomines, M., Briquieu, L., Colin, C., Bouchette, F., Le Duff, M.,  
1225 Blanchemanche, P., 2008. Reconstruction of paleostorm events in a coastal lagoon  
1226 (Hérault, South of France). *Mar. Geol.* 251, 224-232.

1227 Sabatier, P., Dezileau, L., Colin, C., Briquieu, L., Bouchette, F., Martinez, P., Siani, G., Raynal,  
1228 O., Von Grafenstein, U., 2012. 7000 years of paleostorm activity in the NW  
1229 Mediterranean Sea in response to Holocene climate events. *Quat. Res.* 2012, 1-11.

1230 Sadori, L., Giraudi, C., Masi, A., Magny, M., Ortu, E., Zanchetta, G., Izdebski, A., 2016.  
1231 Climate, environment and society in southern Italy during the last 2000 years. A  
1232 review of the environmental, historical and archaeological evidence. *Quat. Sci. Rev.*  
1233 136, 173-188.

1234 Sanchez-Lopez, G., Hernandez, A., Pla-Rabes, S., Trigo, R.M., Toro, M., Granados, I., Saez,  
1235 A., Masqué, P., Pueyo, J.J., Rubio-Inglés, M.J., Giralt, S., 2016. Climate reconstruction for

1236 the last two millennia in central Iberia: The role of East Atlantic (EA), North Atlantic  
1237 Oscillation (NAO) and their interplay over the Iberian Peninsula. *Quat. Sci. Rev.* 149,  
1238 135-150.

1239 Schofield, J.E., Edwards, K.J., Mighall, T.M., Martinez Cortizas, A., Rodriguez-Racedo, J.,  
1240 Cook, G., 2010. An integrated geochemical and palynological study of human impacts,  
1241 soil erosion and storminess from southern Greenland since c. AD 1000. *Palaeogeogr.*  
1242 *Palaeoclimatol. Palaeoecol.* 295, 19-30.

1243 Serreze, M.C., Carse, F., Barry, R.G., Rogers, J.C., 1997. Icelandic Low cyclone activity:  
1244 Climatological features, linkages with the NAO, and relationships with recent Changes  
1245 in the Northern Hemisphere circulation. *J. Climate* 10, 453-464.

1246 Shabbar, A., Huang, J., Higuchi, K., 2001. The relationship between the wintertime North  
1247 Atlantic oscillation and blocking episodes in the North Atlantic. *Int. J. Climatol.* 21,  
1248 355-369.

1249 Shanahan, T.M., Overpeck, J.T., Anchukaitis, K.J., Beck, J.W., Cole, J.E., Dettman, D.L., Peck,  
1250 J.A., Scholz, C.A., King, J.W., 2009. Atlantic forcing of persistent drought in West Africa.  
1251 *Science* 324, 377-380.

1252 Siani, G., Paterne, M., Arnold, M., Bard, E., Métiévier, B., Tisnerat, N., Bassinot, F., 2000.  
1253 Radiocarbon reservoir ages in the Mediterranean Sea and Black Sea. *Radiocarbon* 42  
1254 (2), 271-280.

1255 Sicre, M.-A., Jalali, B., Martrat, B., Schmidt, S., Bassetti, M.-A., Kallel, N., 2016. Sea surface  
1256 temperature variability in the North Western Mediterranean Sea (Gulf of Lion) during  
1257 the Common Era. *Earth Planet. Sci. Lett.* 456, 124-133.

1258 Simms, A.R., Rodriguez, A.B., 2015. The influence of valley morphology on the rate of  
1259 bayhead delta progradation. *J. Sediment. Res.* 85, 38-44.

1260 Simms, A.R., Rodriguez, A.B., Anderson, J.B., 2018. Bayhead deltas and shorelines:  
1261       Insights from modern and ancient examples. *Sediment. Geol.* 374, 17-35.

1262 Somoza, L., Barnolas, A., Arasa, A., Maestro, A., Rees, J.G., Hernandez-Molina, F.J., 1997.  
1263       Architectural stacking patterns of the Ebro delta controlled by Holocene high-  
1264       frequency eustatic fluctuations, delta-lobe switching and subsidence processes.  
1265       *Sediment. Geol.* 117, 11-32.

1266 Sorrel, P., Tessier, B., Demory, F., Delsinne, N., Mouazé, D., 2009. Evidence for millennial-  
1267       scale climatic events in the sedimentary infilling of a macrotidal estuarine system, the  
1268       Seine estuary (NW France). *Quat. Sci. Rev.* 28, 499-516.

1269 Spada, G., Stocchi, P., 2007. SELEN: A Fortran 90 program for solving the “sea-level  
1270       equation”. *Comput. Geosci.* 33, 538-562.

1271 Stanley, J.-D., 2001. Dating modern deltas: progress, problems, and prognostics. *Annu.*  
1272       *Rev. Earth Planet. Sci.* 29, 257-294.

1273 Stanley, J.-D., Warne, A.G., 1994. Worldwide initiation of Holocene marine deltas by  
1274       deceleration of sea-level rise. *Science* 265 (5169), 228-231.

1275 Stanley, J.-D., Hait, A.K., 2000. Deltas, radiocarbon dating, and measurements of sediment  
1276       storage and subsidence. *Geology* 28 (4), 295-298.

1277 Striewski, B., Mayr, C., Flenley, J., Naumann, R., Turner, G., Lücke, A., 2009. Multi-proxy  
1278       evidence of late Holocene human-induced environmental changes at Lake Pupuke,  
1279       Auckland (New Zealand). *Quat. Int.* 202, 69-93.

1280 Stuiver, M., Reimer, P.J., Reimer, R.W., 2019. CALIB 7.1 [WWW program] at  
1281       <http://calib.org>

1282 Toonen, W.H.J., Kleinhans, M.G., Cohen, K.M., 2012. Sedimentary architecture of  
1283       abandoned channel fills. *Earth Surf. Proc. Land.* 37, 459-472.

1284 Toutin-Morin, N., Bonijoly, D., Brocard, C., Broutin, J., Crévola, G., Dardeau, G., Dubar, M.,  
1285 Féraud, J., Giraud, J.D., Godefroy, P., Laville, P., Meinesz, A., 1994. *Notice explicative,*  
1286 *Carte géologique de la France (1/50000), feuille Fréjus-Cannes (1024).* BRGM Editions,  
1287 Orléans, 187 p.

1288 Trigo, I.F., Bigg, G.R., Davies, T.D., 2002. Climatology of cyclogenesis mechanisms in the  
1289 Mediterranean. *Mon. Weather Rev.* 130, 549-569.

1290 Trigo, R.M., Trigo, I.F., DaCamara, C.C., Osborn, T.J., 2004. Climate impact of the European  
1291 winter blocking episodes from the NCEP/NCAR Reanalyses. *Clim. Dynam.* 23, 17-28.

1292 Trouet, V., Esper, J., Graham, N.E., Baker, A., Scourse, J.D., Frank, D.C., 2009. Persistent  
1293 positive North Atlantic Oscillation mode dominated the Medieval Climate Anomaly.  
1294 *Science* 324, 78-80.

1295 Trouet, V., Scourse, J.D., Raible, C.C., 2012. North Atlantic storminess and Atlantic  
1296 Meridional Overturning Circulation during the last Millennium: Reconciling  
1297 contradictory proxy records of NAO variability. *Glob. Planet. Chang.* 84-85, 48-55.

1298 Vacchi, M., Marriner, N., Morhange, C., Spada, G., Fontana, A., Rovere, A., 2016. Multiproxy  
1299 assessment of Holocene relative sea-level changes in the western Mediterranean: Sea-  
1300 level variability and improvements in the definition of the isostatic signal. *Earth Sci.*  
1301 *Rev.* 155, 172-197.

1302 Van der Plicht, J., 2004. Radiocarbon, the calibration curve and Scythian chronology. *In*  
1303 Scott, E.M., Alekseev, A.Y., Zaitseva, G. (Eds.): *Impact of the environment on human*  
1304 *migration in Eurasia.* Springer Netherlands, NATO Science Series, IV Earth and  
1305 Environmental Sciences 42, 45-61.

1306 Véron, A., Morhange, C., Poirier, A., Angeletti, B., Bertoncetto, F., 2018. Geochemical  
1307 markers of human occupation in the lower Argens valley (Fréjus, France): from  
1308 protohistory to Roman times. *J. Archaeol. Sci. Rep.* 17, 242-249.

1309 Vis, G.-J., Bohncke, S.J.P., Schneider, H., Kasse, C., Coenraads-Nederveen, S., Zuurbier, K.,  
1310 Rozema, J., 2010. Holocene flooding history of the Lower Tagus Valley (Portugal). *J.*  
1311 *Quat. Sci.* 25 (8), 1222-1238.

1312 Wassenburg, J.A., Immenhauser, A., Richter, D.K., Niedermayr, A., Riechelmann, S.,  
1313 Fietzke, J., Scholz, D., Jochum, K.P., Fohlmeister, J., Schröder-Ritzrau, A., Sabaoui, A.,  
1314 Riechelmann, D.F.C., Schneider, L., Esper, J., 2013. Moroccan speleothem and tree ring  
1315 records suggest a variable positive state of the North Atlantic Oscillation during the  
1316 Medieval Warm Period. *Earth Planet. Sci. Lett.* 375, 291-302.

1317 Wilhelm, B., Arnaud, F., Sabatier, P., Crouzet, C., Brisset, E., Chaumillon, E., Disnar, J.-R.,  
1318 Guiter, F., Malet, E., Reyss, J.-L., Tachikawa, K., Bard, E., Delannoy, J.-J., 2012. 1400  
1319 years of extreme precipitation patterns over the Mediterranean French Alps and  
1320 possible forcing mechanisms. *Quat. Res.* 78, 1-12.

1321 Wirth, S.B., Glur, L., Gilli, A., Anselmetti, F.S., 2013. Holocene flood frequency across the  
1322 Central Alps – solar forcing and evidence for variations in North Atlantic atmospheric  
1323 circulation. *Quat. Sci. Rev.* 80, 112-128.

1324  
1325

1326 Legend of tables and figures

1327

1328

1329 Table 1. Radiocarbon dates from the Argens River delta system. Elevation in reference to  
1330 LiDAR data (Litto3D, IGN/SHOM). LPT1: La Plaine T1, LPT3: La Plaine T3, TAT2: Théâtre  
1331 d'agglomération T2. \*: age inversion.

1332

1333

1334 Table 2. Nominal relative sea level (RSL) with minimum and maximum errors from  
1335 Vacchi et al. (2016). The RSL prediction was computed using the open source code  
1336 SELEN (Spada and Stocchi, 2007) that employs the ICE-5G (VM2) model from Peltier  
1337 (2004).

1338

1339

1340 Fig. 1. Location of the Argens River in the northwestern Mediterranean (A) and  
1341 topographic and geological setting of the Argens River delta system (B). Coordinate  
1342 system: WGS 1984 World Mercator (A) and RGF 1993 Lambert-93 (B). ITCZ:  
1343 intertropical convergence zone. 1, 2: Durance River sites (Arnaud-Fassetta et al., 2010;  
1344 Benito et al., 2015a). Marine records of terrigenous material in sediments from the  
1345 western Mediterranean basin: KSGC-31 site (Jalali et al., 2016); MD99-2343 site (Frigola  
1346 et al., 2007); 305G, 306G, 384B and 436B sites (NietoMoreno et al., 2011, 2013a, 2013b);  
1347 DP30 site (Goudeau et al., 2014, 2015). References of published cores and archaeological  
1348 surveys: Dubar (2004) for Verteil core, Allinne et al. (2006) for ESC1 core, Devillers and  
1349 Bonnet (2006) for VIL2 core, Excoffon et al. (2006) and Devillers et al. (2007) for  
1350 Théâtre d'agglomération T2 archaeological survey, Excoffon et al. (2010) for Villa



1351 Romana archaeological survey, Bony et al. (2011) for FIX, FXI and SC6 cores, Bertonecello  
1352 et al. (2014a) for PL1 and PAL1 cores, Bertonecello et al. (2016) for La Plaine T1-T3  
1353 archaeological survey.

1354

1355

1356 Fig. 2. Stratigraphy, magnetic susceptibility, geochemistry and malacofauna of BN1 core  
1357 in the Argens River delta system. Vertical dashed lines correspond to the mean values of  
1358 variables.

1359

1360

1361 Fig. 3. Stratigraphy, magnetic susceptibility, geochemistry and malacofauna of BN5 core  
1362 in the Argens River delta system. Vertical dashed lines correspond to the mean values of  
1363 variables.

1364

1365

1366 Fig. 4. Malacological diagram of BN1 core. Main environmental conditions inferred from  
1367 a cluster analysis by constrained incremental sum of squares (CONISS) with a  
1368 dissimilarity coefficient corresponding to Edwards and Cavalli-Sforza's chord distance  
1369 (Grimm, 1987).

1370

1371

1372 Fig. 5. Malacological diagram of BN5 core. Main environmental conditions inferred from  
1373 a cluster analysis by constrained incremental sum of squares (CONISS) with a  
1374 dissimilarity coefficient corresponding to Edwards and Cavalli-Sforza's chord distance  
1375 (Grimm, 1987).

1376

1377

1378 Fig. 6. 2D age-elevation models in the coastal plain of the Argens River delta system. The  
1379 data used in the age-elevation models correspond to the median probability of  
1380 calibrated ages (white dot) from the compilation of radiocarbon ages available in the  
1381 Argens River delta system (Table 1) and to modern elevation based on LiDAR data  
1382 (Litto3D, IGN/SHOM) for the year 2015 (blue triangle). Numbers in brackets represent  
1383 the 2- $\sigma$  uncertainty interval of calibrated ages (Table 1). The radiocarbon ages in red  
1384 were discarded to avoid age reversals (see explanation in text). References for  
1385 radiocarbon ages, lithology and depositional environment (if available): Dubar (2004)  
1386 for Verteil core, Allinne et al. (2006) for ESC1 core, Devillers and Bonnet (2006) for VIL2  
1387 core, Devillers et al. (2007) for Théâtre d'agglomération T2 archaeological survey,  
1388 Excoffon et al. (2010) for Villa Romana archaeological survey, Bertoncello et al. (2014a)  
1389 for PL1 and PAL1 cores, Bertoncello et al. (2016) for La Plaine T1 and T3 archaeological  
1390 surveys, and this study for BN1 and BN5 cores. The data point for Villa Romana was  
1391 estimated from the reconstruction of the shoreline around 2000 cal yr BP based on  
1392 archaeological data, radiocarbon ages and relative sea level reconstruction (Excoffon et  
1393 al., 2010; Vacchi et al., 2016). Location of age-elevation models A1-3 in Fig. 1B. Models  
1394 interpolated with a thin plate spline kernel function and an 8-sector neighbourhood  
1395 search algorithm. The isochrones of the unconfined bayhead delta were obtained by  
1396 shifting the LiDAR data along the BN5 age-elevation model. (For interpretation of the  
1397 references to colour in this figure legend, the reader is referred to the web version of  
1398 this article.)

1399

1400

1401 Fig. 7. Interpolated maps of sediment thickness in the Argens River delta system over  
1402 the past 2500 years. LPT1 and LPT3: La Plaine T1 and T3 archaeological surveys, TAT2:  
1403 Théâtre d'agglomération T2 archaeological survey, VR: Villa Romana archaeological  
1404 survey. Models interpolated with a multiquadratic kernel function and an 8-sector  
1405 neighbourhood search algorithm.

1406

1407

1408 Fig. 8. Palaeoelevation in the Argens River delta system over the past 2500 years. LPT1  
1409 and LPT3: La Plaine T1 and T3 archaeological surveys, TAT2: Théâtre d'agglomération  
1410 T2 archaeological survey, VR: Villa Romana archaeological survey. The past sea levels  
1411 used in the elevation models are based on the relative sea level (RSL) in the western  
1412 Ligurian Sea determined by the ICE-5G (VM2) geophysical model (Peltier, 2004) for the  
1413 last 2500 years (Table 2). In this area, a good fit between the model and available  
1414 geological sea level proxies was observed along the whole Holocene (Vacchi et al., 2016).  
1415 The reconstructed RSL at 2000 cal yr BP is consistent with the Roman sea level deduced  
1416 from marine encrustation found on archaeological harbour structures, a very robust  
1417 methodology to infer the RSL position in the Mediterranean Sea (Morhange and  
1418 Marriner, 2015; Vacchi et al., 2016). The RSL in the *Forum Iulii* harbour (Fig. 1B) was  
1419 estimated at  $-40 \pm 10$  cm (Morhange et al., 2013) or  $-33 \pm 6$  cm (Devillers et al., 2007)  
1420 between the first century BCE and the first century CE.

1421

1422

1423 Fig. 9. Evolution of sediment flux and fluvial activity in the Argens River delta system  
1424 (ARDS) and comparison with riverine flooding frequency in the southern French Alps  
1425 over the past 2500 years. (a) Sediment fluxes calculated for each 500-year interval by

1426 estimating the volume of sediment using the ArcGIS 10 Surface Volume tool with either  
1427 (1) the elevation models in Fig. 8 and reference planes corresponding to the mean  
1428 relative sea level from Vacchi et al. (2016) for each 500-year interval for the confined  
1429 bayhead delta, or (2) the LiDAR data shifted along the BN5 age-elevation model (Fig. 6,  
1430 age profile A1) and a reference plane at 20 m below present sea level for the unconfined  
1431 bayhead delta. (b) Proxy records of riverine input and fluvial activity corresponding to  
1432 the average of the standard scores of Si/Al, K/Al and Rb/Al ratios from BN1 core with an  
1433 age scale established by using AnalySeries 2.0 (Paillard et al., 1996). (c) Proxy records of  
1434 riverine input and fluvial activity corresponding to the average of the standard scores of  
1435 Si/Al, K/Al and Rb/Al ratios from BN5 core with an age scale established by using  
1436 AnalySeries 2.0 (Paillard et al., 1996). (d) Periods of relatively high flood frequency of  
1437 the lower Durance River and its tributaries (site 1 in Fig. 1A) in the southern French  
1438 Alps (Arnaud-Fassetta et al., 2010; Benito et al., 2015a). (e) Periods of relatively high  
1439 flood frequency of the middle Durance River and its tributaries (site 2 in Fig. 1A) in the  
1440 southern French Alps (Arnaud-Fassetta et al., 2010; Benito et al., 2015a). (f) Relative  
1441 cumulative probability density function of radiocarbon dates from flood and extreme  
1442 fluvial event units of rivers in southeastern France (Fig. 1A) (Benito et al., 2015a). IACP:  
1443 Iron Age Cold Period, RWP: Roman Warm Period, DACP: Dark Ages Cold Period, MWP:  
1444 Medieval Warm Period, LIA: Little Ice Age, GW: Global Warming.

1445

1446

1447 Fig. 10. Comparison of sediment flux and fluvial activity in the Argens River delta system  
1448 (ARDS) with geomorphic factors and climate proxy records over the last 2500 years. (a)  
1449 Mean slope of the ARDS longitudinal gradient between Verteil and BN5 from age profiles  
1450 in Fig. 6. (b) Volume of accommodation space of the ARDS estimated using the ArcGIS 10

1451 Surface Volume tool with the elevation models in Fig. 8 and reference planes  
1452 corresponding to the relative sea level from Vacchi et al. (2016). (c) Subaqueous  
1453 sediment flux in the ARDS with an error range of  $\pm 20\%$ . (d) Subaerial sediment flux in  
1454 the ARDS with an error range of  $\pm 20\%$ . (e) Fluvial activity in the easternmost part of the  
1455 lower Argens valley corresponding to the average of the standard scores of fluvial  
1456 activity at BN1 and BN5 (Fig. 9b-c) resampled at a 5-years interval by linear  
1457 interpolation using AnalySeries 2.0 (Paillard et al., 1996), along with period of autogenic  
1458 control (see section 7.2). (f) Mean band width of three radiometrically dated  
1459 speleothems from the Uamh an Tartair cave in northwestern Scotland (Fig. 1A) (Proctor  
1460 et al., 2002). (g) Potential leading mode of atmospheric circulation in Europe (see  
1461 section 7.3). (h) Alkenone-based sea surface temperature (SST) in the northwestern  
1462 Mediterranean with cold relapse episodes (CR4-6) from the KSCG-31 core in the Gulf of  
1463 Lions (Fig. 1A) (Jalali et al., 2016). (i) Storm activity in southeastern France from the  
1464 sedimentary record of the Bagnas lagoon (Fig. 1A) (Degeai et al., 2015). (j) Storm  
1465 activity in southeastern France from the sedimentary record of the Pierre Blanche  
1466 lagoon (Fig. 1A) (Sabatier et al., 2012). (k) Storm activity from sedimentary records in  
1467 the Seine River estuary in northwestern France (Fig. 1A) (Sorrel et al., 2009). (l)  
1468 Potential second or third mode of atmospheric circulation in Europe (see section 7.3).  
1469 (m) 5-yr averaged oxygen isotope record of authigenic carbonate from Lake Bosumtwi  
1470 in Ghana (Fig. 1A) (Shanahan et al., 2009). NAO: North Atlantic oscillation, EA: East  
1471 Atlantic pattern, EA/WR: East Atlantic/West Russian pattern, IACP: Iron Age Cold  
1472 Period, RWP: Roman Warm Period, DACP: Dark Ages Cold Period, MWP: Medieval Warm  
1473 Period, LIA: Little Ice Age, GW: Global Warming.

1474

1475

1476 Fig. 11. Late Holocene atmospheric circulation patterns and climatic conditions in the  
1477 North Atlantic and Europe during the periods of high fluvial activity driven by climate  
1478 change in the Argens lower valley. Empirical orthogonal functions (EOF1-3) calculated  
1479 from sea level pressure reconstructed by Luterbacher et al. (2002) for the period 1500-  
1480 1999 CE. 1: Argens River delta system, 2: Gulf of Lions, 3: Bagnas and Pierre Blanche  
1481 lagoons, 4: Seine River estuary, SST: sea surface temperature, NAO: North Atlantic  
1482 oscillation, EA: East Atlantic pattern, EA/WR: East Atlantic/West Russian pattern, ITCZ:  
1483 intertropical convergence zone, IACP: Iron Age Cold Period, RWP: Roman Warm Period,  
1484 DACP: Dark Ages Cold Period, LIA: Little Ice Age.

1485

Core or trench	Elevation (m)	Laboratory code	Material	<sup>14</sup> C age (BP)	Reference	2-σ interval of calibrated age (cal yr BP)	Median probability of calibrated age (cal yr BP)
BN1	0.30	Poz-81546	Charcoal	375 ± 30	This study	504-318	442
BN1	-3.60	Poz-81547	Charcoal	2520 ± 30	This study	2744-2492	2595*
BN1	-5.60	Poz-81608	Charcoal	2215 ± 30	This study	2322-2151	2231*
BN1	-7.00	Poz-81548	Charcoal	3330 ± 35	This study	3678-3467	3565*
BN1	-8.60	Poz-81549	Charcoal	2085 ± 30	This study	2143-1990	2058
BN1	-10.10	Poz-81550	Charcoal	2480 ± 30	This study	2723-2385	2585
BN5	-7.86	Lyon-13936	Wood	2055 ± 30	This study	2118-1934	2023*
BN5	-9.98	Lyon-13937	Wood	1975 ± 30	This study	1993-1871	1925
BN5	-12.33	Lyon-13938	Wood	2175 ± 30	This study	2310-2072	2231
BN5	-13.67	Lyon-13939	Wood	2195 ± 30	This study	2313-2133	2237
ESC1	0.18	Poz-12168	Seed	680 ± 30	Allinne et al. (2006)	680-561	652
ESC1	-1.57	Poz-12167	Seed	2535 ± 30	Allinne et al. (2006)	2747-2495	2625
ESC1	-2.52	Poz-12166	Seed	3735 ± 35	Allinne et al. (2006)	4227-3980	4089*
ESC1	-4.82	Poz-9593	Charcoal	3535 ± 35	Allinne et al. (2006)	3904-3702	3816
LPT1	3.44	Poz-78590	Charcoal	155 ± 30	Bertoncello et al. (2016)	284-0	174
LPT1	3.14	Poz-78591	Charcoal	175 ± 30	Bertoncello et al. (2016)	293-0	180
LPT1	2.44	Poz-78589	Charcoal	1315 ± 30	Bertoncello et al. (2016)	1295-1183	1259
LPT3	3.05	Poz-78593	Charcoal	4125 ± 30	Bertoncello et al. (2016)	4817-4531	4667*
LPT3	2.45	Poz-80846	Charcoal	960 ± 50	Bertoncello et al. (2016)	960-764	859
PAL1	-0.74	Lyon-5430	Seed	1075 ± 35	Bertoncello et al. (2014a)	1057-930	982
PAL1	-1.84	Lyon-5431	Seed	1285 ± 35	Bertoncello et al. (2014a)	1294-1097	1232*

PAL1	-2.34	Lyon-5432	Seed	1285 ± 35	Bertoncello et al. (2014a)	1294-1097	1232
PAL1	-8.84	Lyon-5061	Seed	2145 ± 30	Bertoncello et al. (2014a)	2304-2009	2137
PAL1	-14.34	Lyon-5062	Seed	2210 ± 30	Bertoncello et al. (2014a)	2320-2149	2232
PAL1	-17.34	Lyon-5433	Seed	2800 ± 40	Bertoncello et al. (2014a)	2998-2791	2904
PL1	1.49	Lyon-4223	Charcoal	1540 ± 35	Bertoncello et al. (2014a)	1525-1356	1448
PL1	-1.21	Lyon-4221	Seed	2515 ± 40	Bertoncello et al. (2014a)	2746-2467	2593*
PL1	-1.76	Lyon-4228	Seed	2510 ± 30	Bertoncello et al. (2014a)	2740-2490	2590*
PL1	-3.41	Lyon-4226	Charcoal	3120 ± 35	Bertoncello et al. (2014a)	3442-3234	3340*
PL1	-3.56	Lyon-5434	Seed	2395 ± 35	Bertoncello et al. (2014a)	2687-2345	2425
PL1	-4.31	Lyon-4225	Charcoal	2450 ± 30	Bertoncello et al. (2014a)	2704-2361	2528
PL1	-6.76	Lyon-4224	Seed	2490 ± 40	Bertoncello et al. (2014a)	2738-2381	2583
PL1	-7.51	Lyon-5435	Charcoal	4200 ± 45	Bertoncello et al. (2014a)	4851-4584	4730*
PL1	-8.81	Lyon-4222	Charcoal	2820 ± 35	Bertoncello et al. (2014a)	3057-2846	2924*
PL1	-10.06	Lyon-4219	Charcoal	2610 ± 40	Bertoncello et al. (2014a)	2843-2540	2749
TAT2	-0.33	Poz-14372	Marine shell	2345 ± 30	Devillers et al. (2007)	2087-1888	1983
Verteil	-2.41	Ly 5889	Peat	3050 ± 75	Dubar et al. (2004)	3443-3008	3247
VIL2	-2.25	Poz-10916	Charcoal	915 ± 30	Devillers and Bonnet (2006)	920-762	848
VIL2	-2.90	Poz-10917	Charcoal	1340 ± 30	Devillers and Bonnet (2006)	1305-1185	1280
VIL2	-5.65	Poz-10918	Charcoal	2325 ± 30	Devillers and Bonnet (2006)	2426-2208	2345
VIL2	-7.75	Poz-10922	Marine shell	5190 ± 30	Devillers and Bonnet (2006)	5634-5478	5571



1488  
1489

1490 Table 2

1491

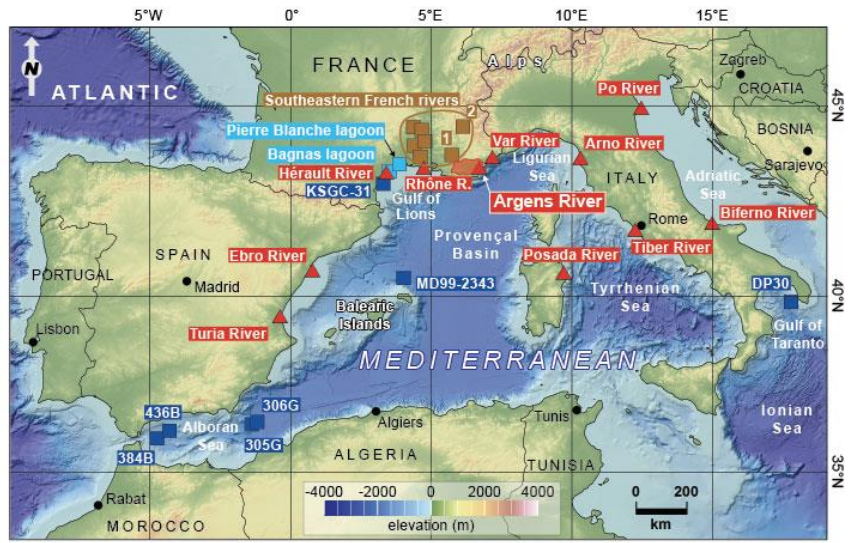
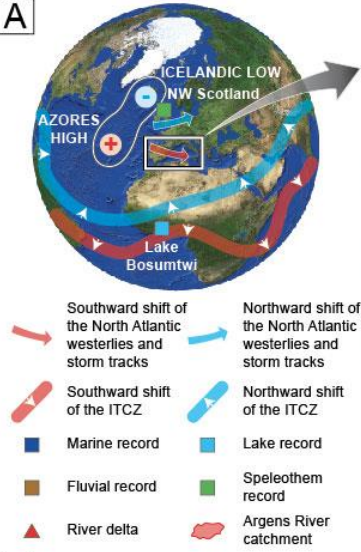
Age (cal yr BP)	Minimum RSL (m)	Nominal RSL (m)	Maximum RSL (m)
0	0.00	0.00	0.00
500	-0.14	-0.07	0.06
1000	-0.28	-0.13	0.12
1500	-0.43	-0.20	0.19
2000	-0.58	-0.28	0.26
2500	-0.78	-0.38	0.32

1492

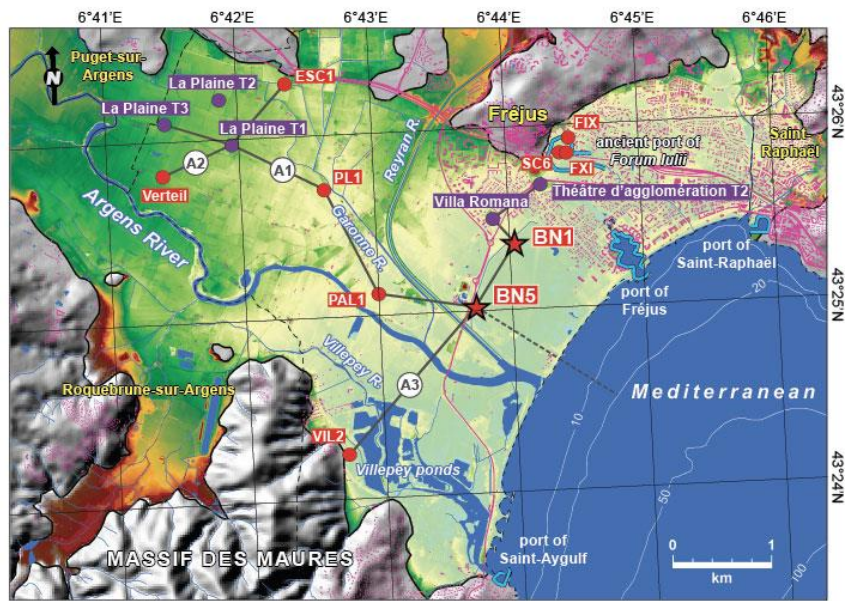
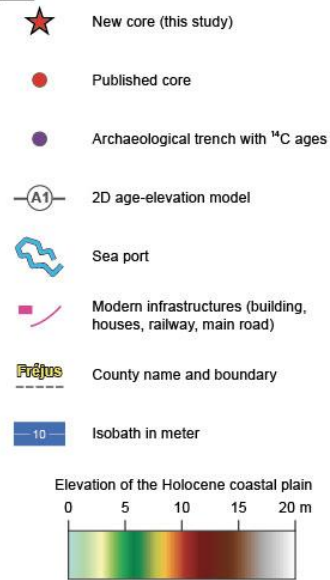
1493

1494

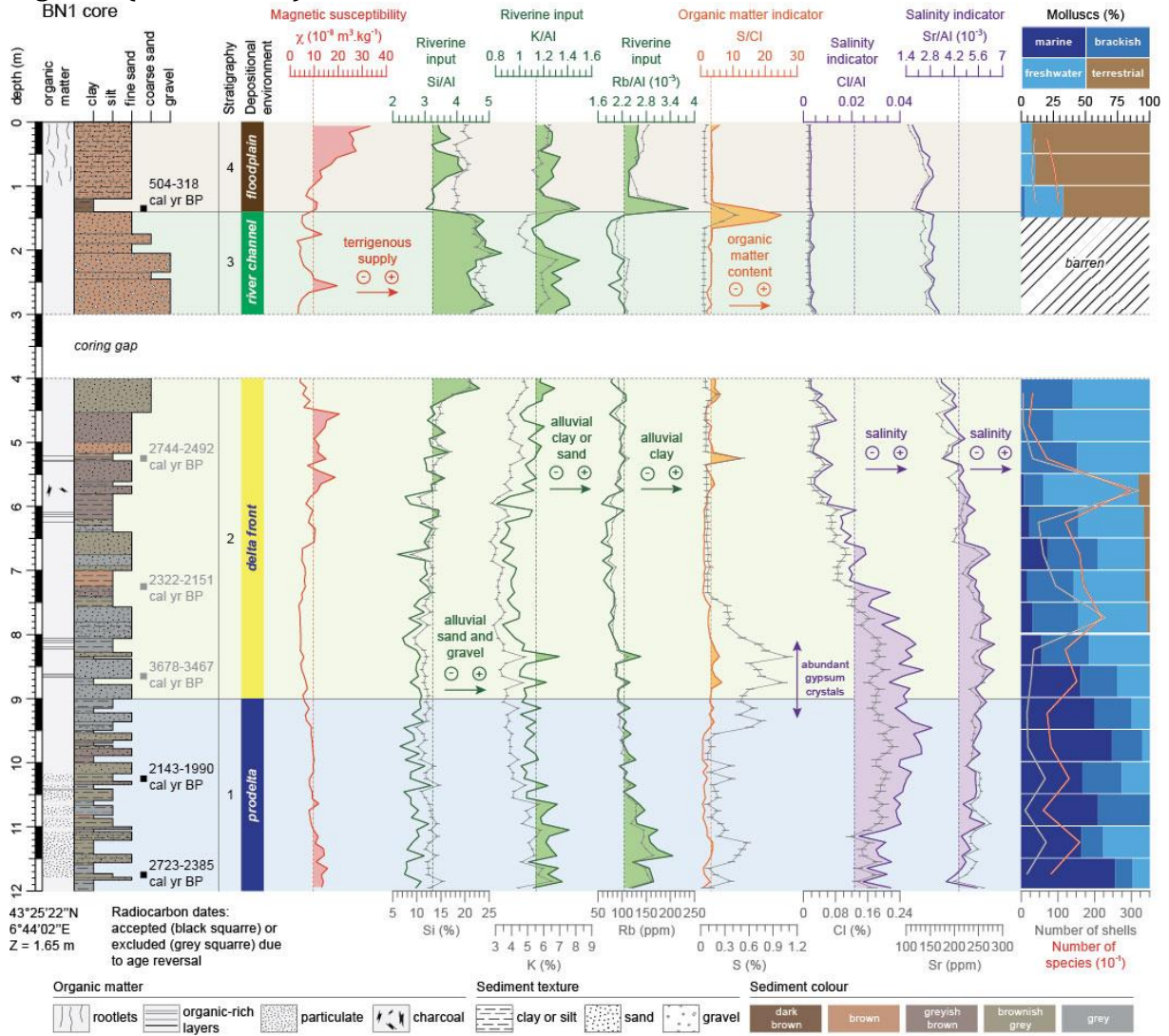
A



B

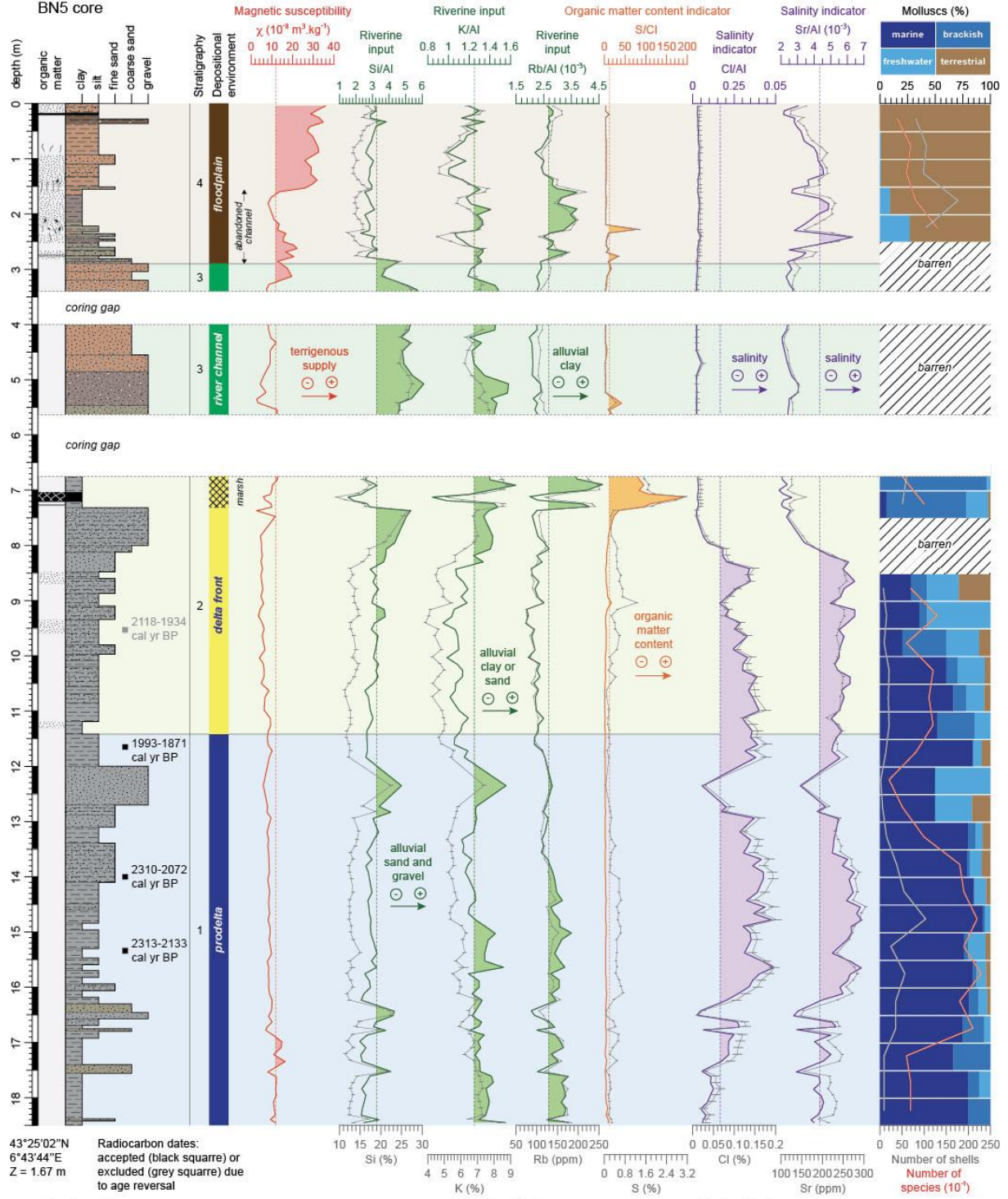


1497 Figure 2 (two-column)

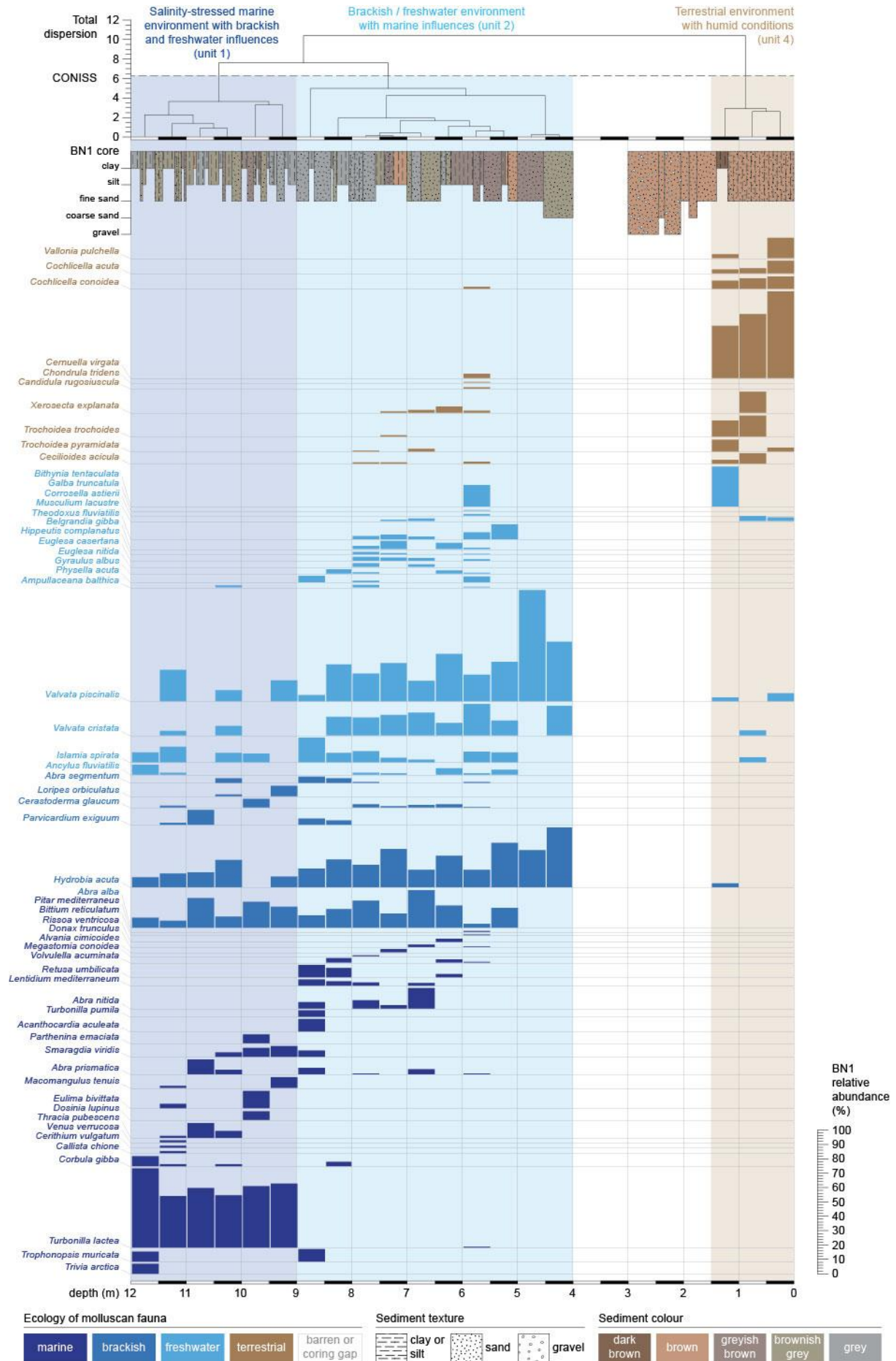


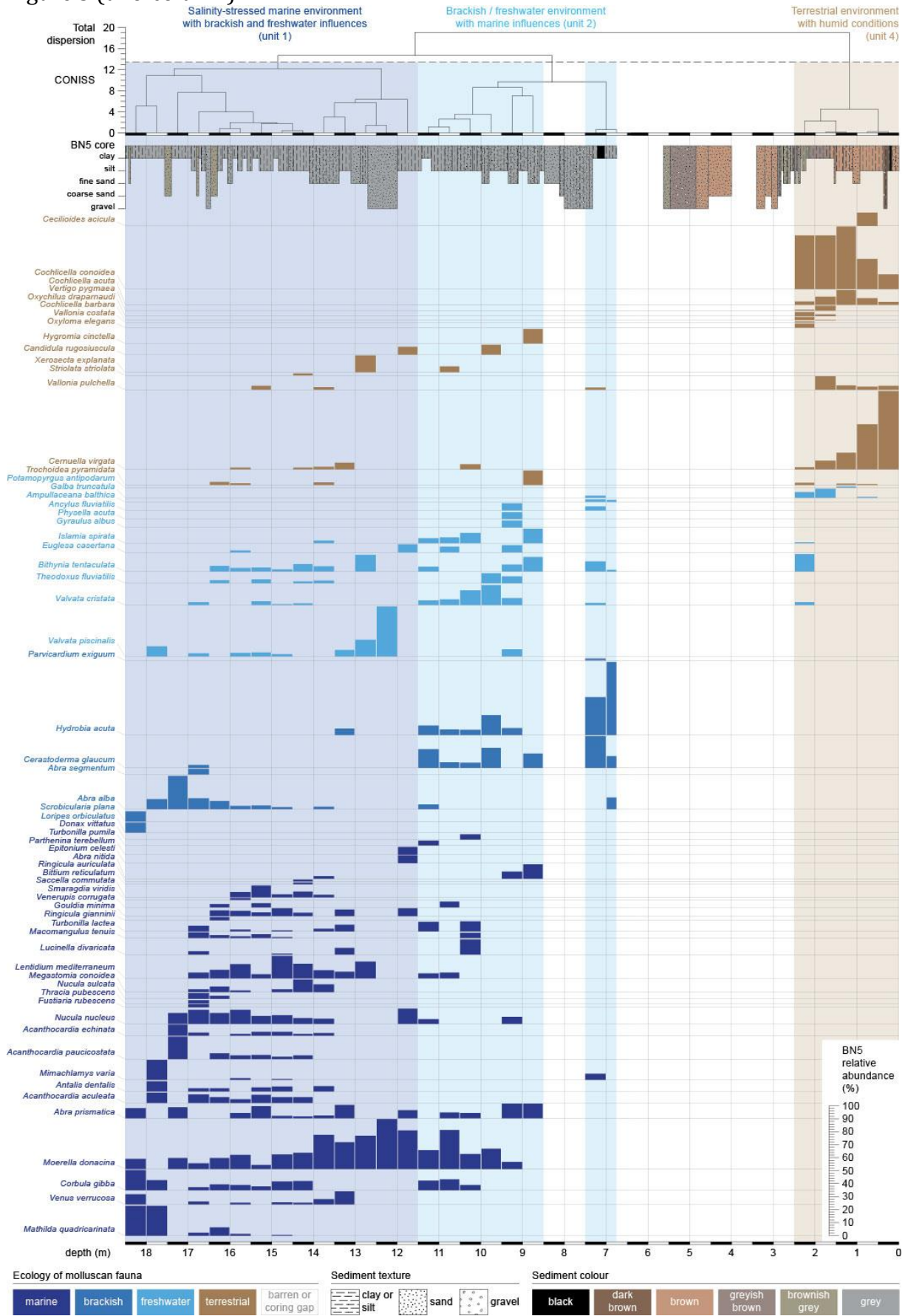
1498

1499 Figure 3 (two-column)  
BN5 core



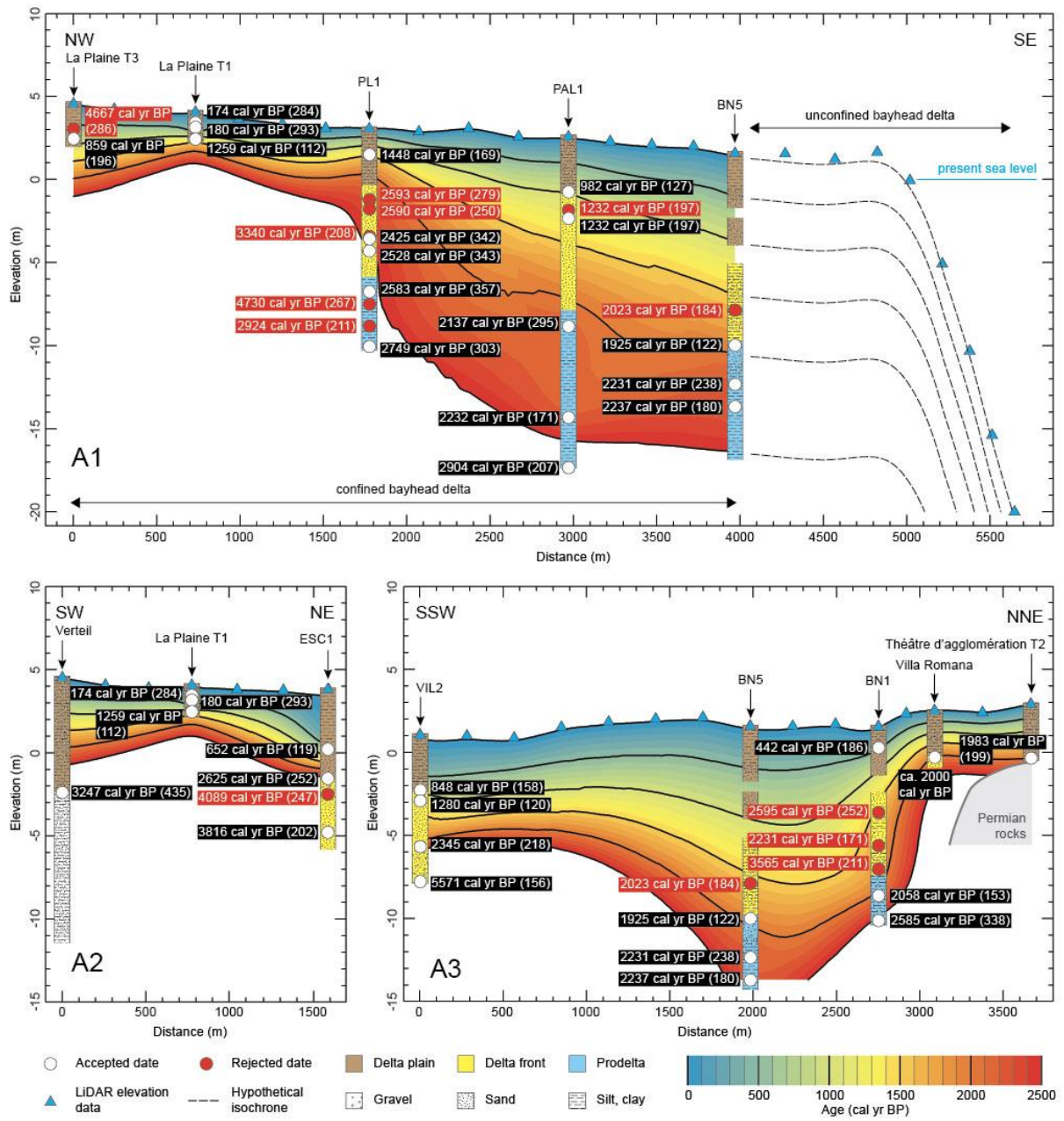
1501 Figure 4 (two-column)

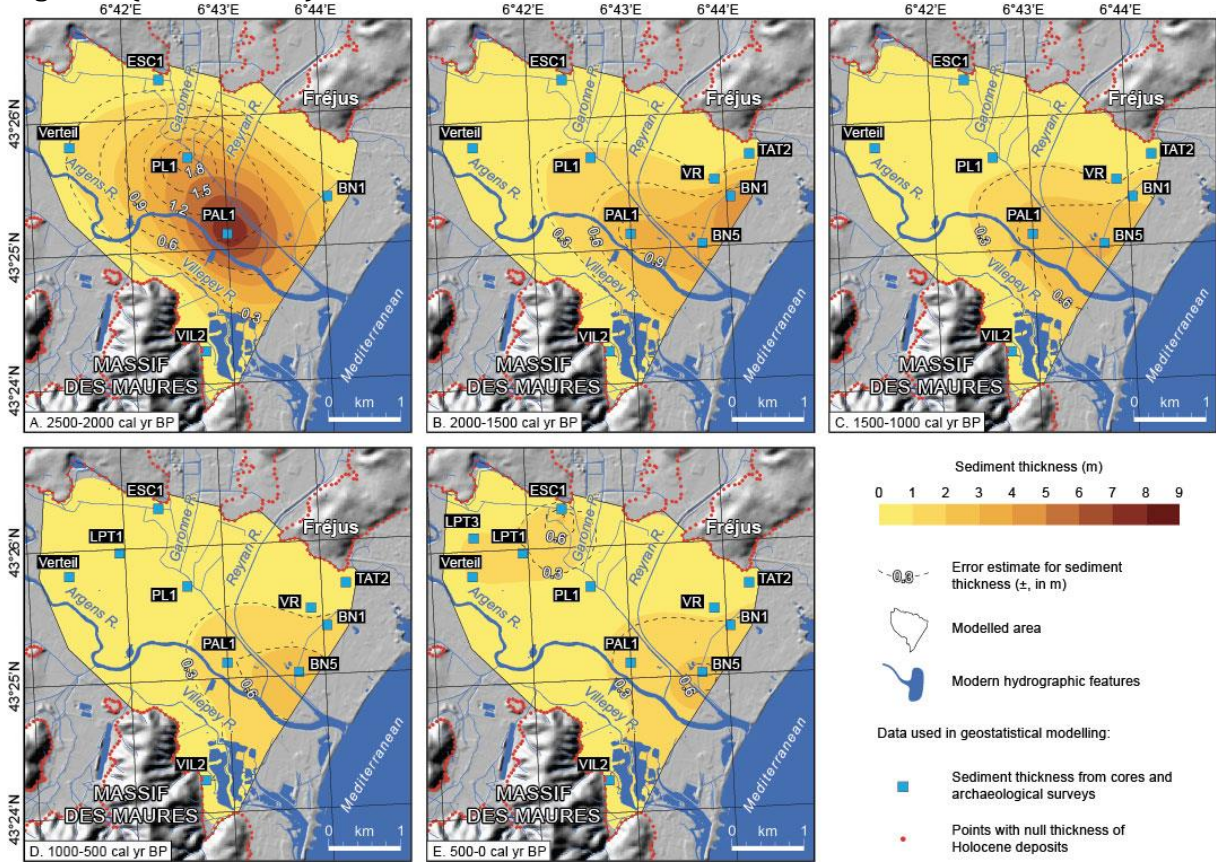


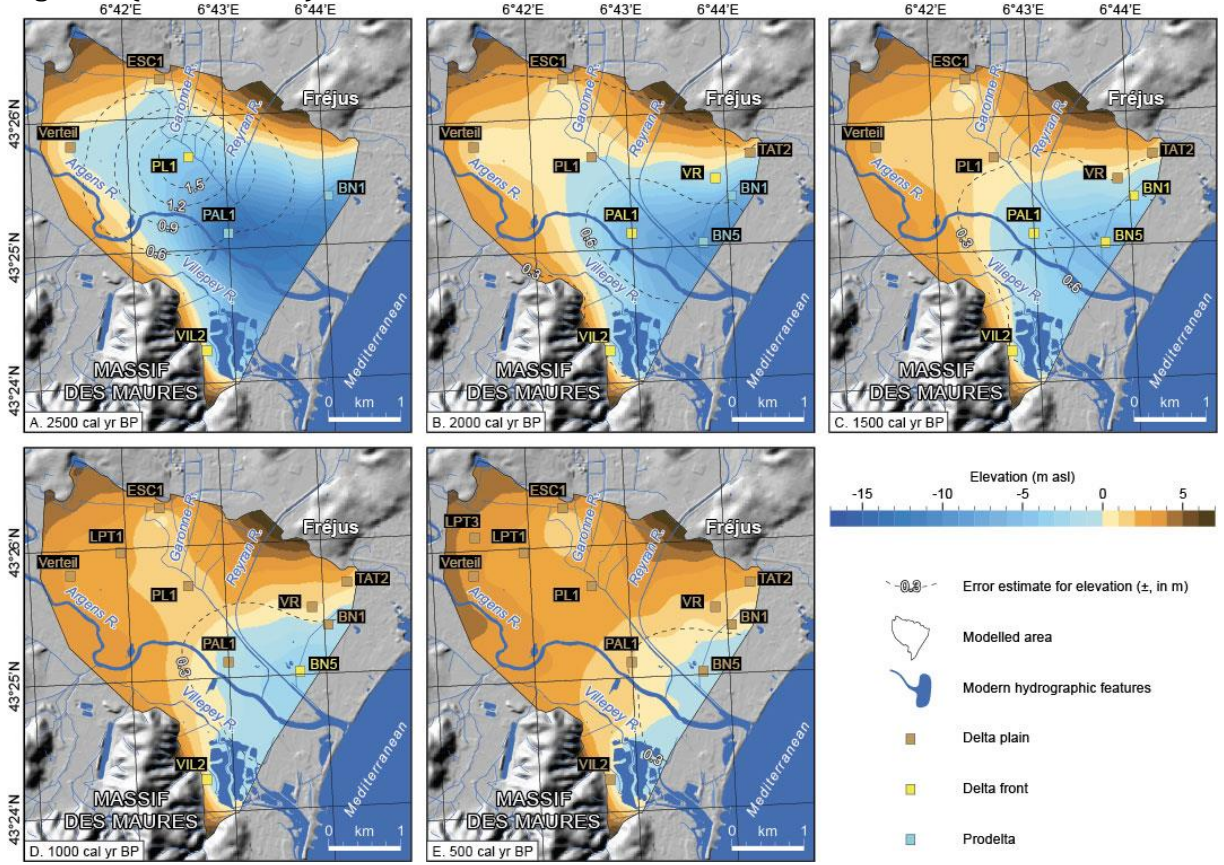




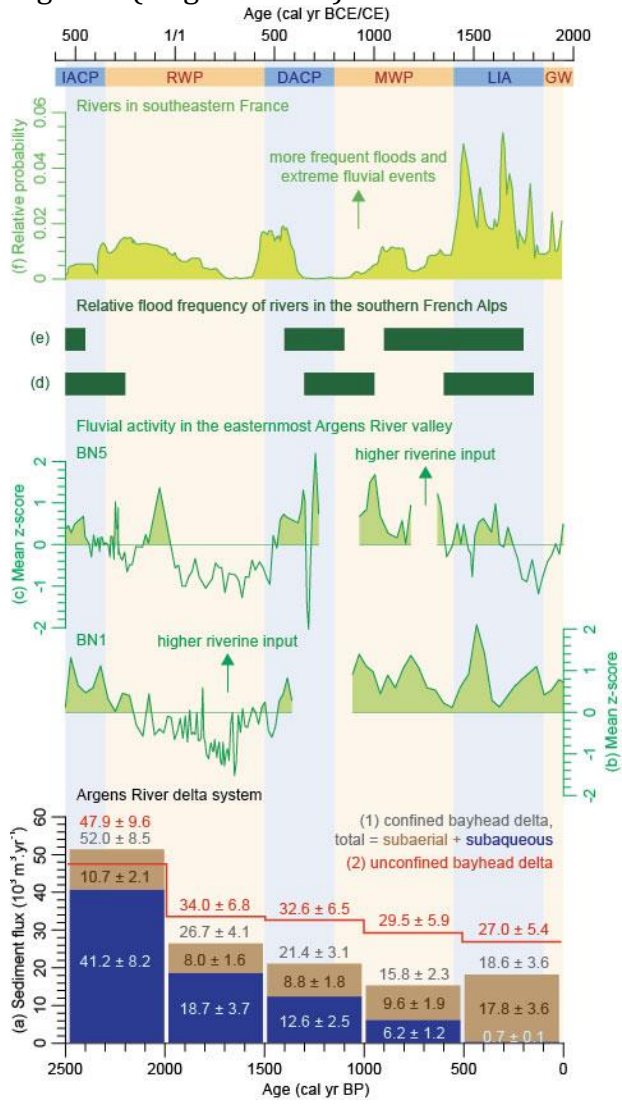
1505 Figure 6 (two-column)





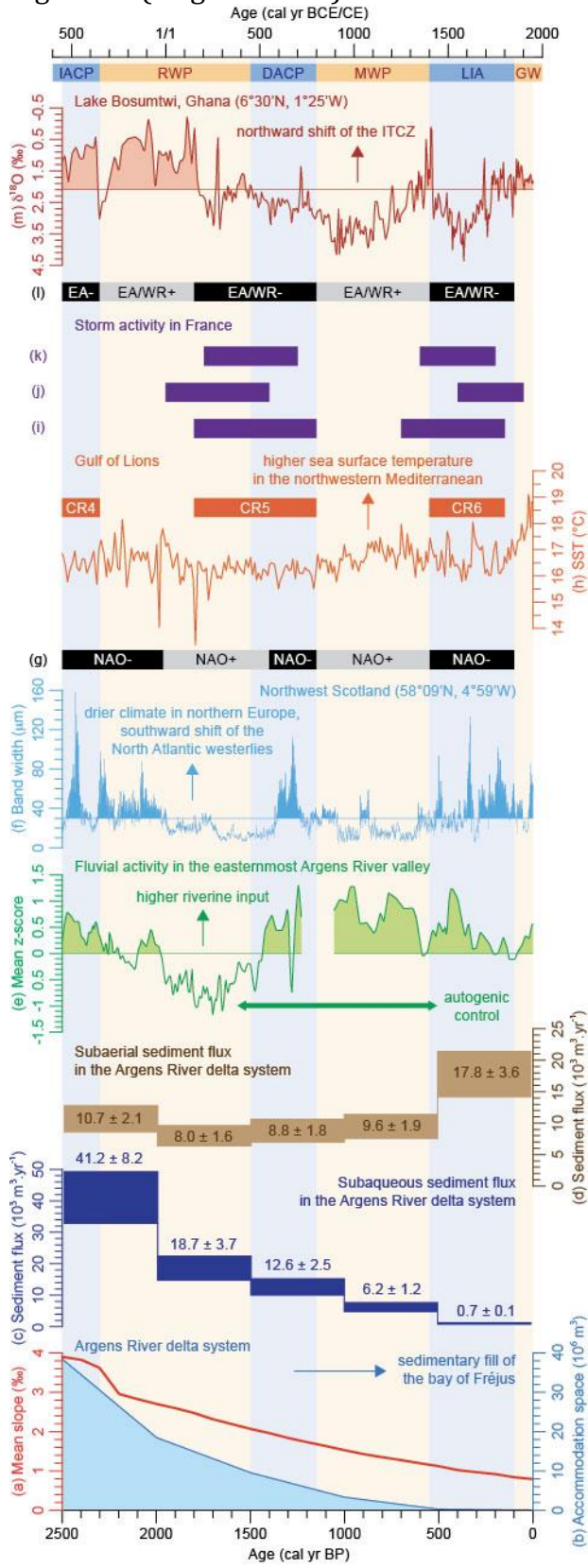


1511 Figure 9 (single column)

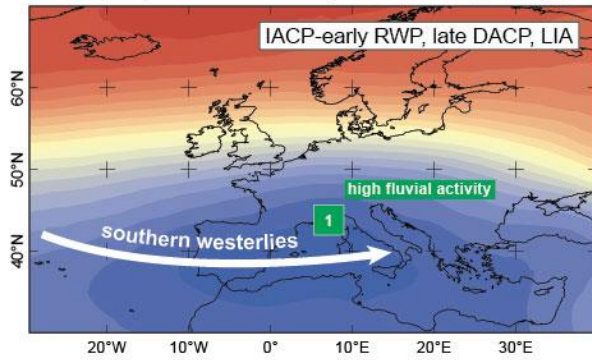


1512

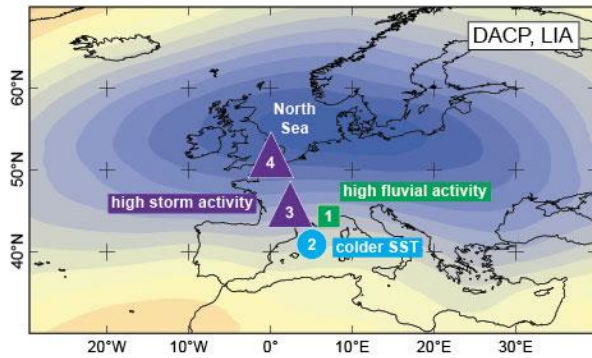
1513 Figure 10 (single column)



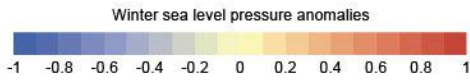
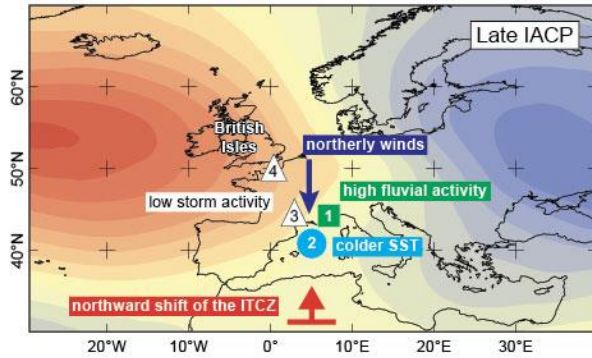
1515 Figure 11 (single column)  
 A. EOF1 (51%) NAO-like pattern in its negative phase



B. EOF2 (20%) EAWR pattern in its negative phase



C. EOF3 (14%) EA pattern in its negative phase



1516  
 1517